

Panchromatic HST/WFC3 Imaging Studies of Young, Rapidly Evolving Planetary Nebulae. I. NGC 6302

JOEL H. KASTNER,^{1,2} PAULA MORAGA,² BRUCE BALICK,³ JESSE BUBLITZ,² RODOLFO MONTEZ JR.,⁴ ADAM FRANK,⁵ AND
ERIC BLACKMAN⁵

¹*Center for Imaging Science and Laboratory for Multiwavelength Astrophysics, Rochester Institute of Technology, Rochester NY 14623, USA; jhk@cis.rit.edu*

²*School of Physics and Astronomy and Laboratory for Multiwavelength Astrophysics, Rochester Institute of Technology*

³*Department of Astronomy, University of Washington, Seattle WA, 98195, USA*

⁴*Center for Astrophysics — Harvard & Smithsonian, Cambridge MA, 02138, USA*

⁵*Department of Physics & Astronomy, University of Rochester, Rochester NY, 14627, USA*

ABSTRACT

We present the results of a comprehensive, near-UV-to-near-IR Hubble Space Telescope WFC3 imaging study of the young planetary nebula (PN) NGC 6302, the archetype of the class of extreme bi-lobed, pinched-waist PNe that are rich in dust and molecular gas. The new WFC3 emission-line image suite clearly defines the dusty toroidal equatorial structure that bisects NGC 6302’s polar lobes, and the fine structures (clumps, knots, and filaments) within the lobes. The most striking aspect of the new WFC3 image suite is the bright, S-shaped 1.64 μm [Fe II] emission that traces the southern interior of the east lobe rim and the northern interior of the west lobe rim, in point-symmetric fashion. We interpret this [Fe II] emitting region as a zone of shocks caused by ongoing, fast ($\sim 100 \text{ km s}^{-1}$), collimated, off-axis winds from NGC 6302’s central star(s). The [Fe II] emission and a zone of dusty, N- and S-rich clumps near the nebular symmetry axis form wedge-shaped structures on opposite sides of the core, with boundaries marked by sharp azimuthal ionization gradients. Comparison of our new images with earlier HST/WFC3 imaging reveals that the object previously identified as NGC 6302’s central star is a foreground field star. Shell-like inner lobe features may instead pinpoint the obscured central star’s actual position within the nebula’s dusty central torus. The juxtaposition of structures revealed in this HST/WFC3 imaging study of NGC 6302 presents a daunting challenge for models of the origin and evolution of bipolar PNe.

Keywords: Planetary nebulae (1249), Stellar mass loss (1613), Jets (870), Circumstellar matter (241)

1. INTRODUCTION

Planetary nebulae (PNe) are the near-endpoints of stellar evolution for intermediate-mass ($\sim 1\text{--}8 M_{\odot}$) stars. Each PN provides a snapshot of the brief ($\sim 10^4$ yr duration) stage in which the outflowing, dusty circumstellar envelope of an asymptotic giant branch (AGB) star is ionized by its newly unveiled core, itself a future white dwarf (e.g., Schoenberner 1986). PNe thereby offer our last and arguably best look at the products of intermediate-mass stellar nucleosynthesis, just before that material is incorporated into the ISM (Kwitter et al. 2014).

Though best known as photogenic, $\sim 10^4$ K optical emission line sources, a subset of PNe — those with pinched-waist, bipolar structures — retain significant masses of cold (< 100 K), dense ($\sim 10^4\text{--}10^6 \text{ cm}^{-3}$) molecular gas and dust that is irradiated, shocked, and continuously reshaped from within by UV and winds from hot ($\sim 30\text{--}200$ kK) central stars (e.g., Huggins et al. 1996; Kastner et al. 1996; Bachiller et al. 1997; Huggins et al. 2005; Bublitz et al. 2019, and refs. therein). As the descendants of relatively massive progenitor stars (Corradi & Schwarz 1995), many of these dusty, molecule-rich, bipolar PNe are also the youngest and most morphologically and dynamically extreme objects (Kastner et al. 1996; Balick & Frank 2002; Sahai et al. 2011).

An effective way to study PN-shaping stellar winds, and the rapid evolution of these winds, is to observe their impacts on the slower but denser post-AGB material downstream. Classical PN shaping theory implicitly or explicitly posits that the driving force of the active winds from the present-day central stars of PNe is isotropic radiative momentum (Kwok et al. 1978). However, the highly non-isotropic lobes of bipolar PNe must be formed in some other manner, via the ram pressure in collimated winds or jets of some sort (e.g., Bujarrabal et al. 2001; Akashi & Soker 2018; Balick et al. 2019). Evidence has steadily accumulated that such collimated outflows are ultimately due to the influence of an (interacting) binary companion to the mass-losing central star (e.g., Jones & Boffin 2017; De Marco & Izzard 2017, and references therein), with processes such as common envelope (CE) evolution (e.g., Livio et al. 1979; Soker 2004; García-Segura et al. 2018; Zou et al. 2020) or jets associated with a companion star’s accretion disk (e.g., Morris 1987; Soker & Livio 1994; Chen et al. 2017) providing the mass launching and collimation mechanisms.

Narrow-band imaging with the *Hubble Space Telescope* (HST) has long played a fundamental role in advancing our understanding of these and other potential PN shaping mechanisms (e.g., Sahai & Trauger 1998). As HST neared the end of its third decade in operation, however, the community of PNe researchers had yet to take full advantage of the potential of its most capable imaging instrument, the Wide Field Camera 3 (WFC3). This changed in HST Cycle 27, when we used HST/WFC3 to obtain the first comprehensive, contemporaneous sets of near-UV through near-IR (243 nm to 1.6 μm) emission-line images of two especially structurally rich PNe, NGC 7027 and NGC 6302 (see Kastner et al. 2020, for an initial overview of these HST/WFC3 imaging surveys). As we demonstrate in this paper, the broad, contemporaneous wavelength coverage of these WFC3 image suites yields full-nebula emission line image overlays and line ratio maps at $\sim 0.1''$ resolution that are free from distortions and artifacts caused by nebular proper motions or cross-instrument calibration uncertainties (among other potential pitfalls).

The subject of this paper, NGC 6302 (the Butterfly), is the archetype of the class of extreme bi-lobed, pinched-waist PNe that are rich in dust and molecular gas. As of this writing, NGC 6302 had been featured or mentioned in more than 750 papers, according to *simbad*. Its bipolar lobes are very bright and rich in emission lines, spanning a remarkably broad range of ionization states, from the far-UV through the mid-IR (e.g., Casassus et al. 2000; Feibelman 2001; Molster et al. 2001; Groves et al. 2002). Indeed, NGC 6302 has long served as an exemplar for studies of high-excitation PNe (e.g., Aller et al. 1981), with estimates of its central star temperature ranging from 220–250 kK (Casassus et al. 2000; Wright et al. 2011) to as high as ~ 400 kK (Ashley & Hyland 1988). Expansion parallax distance estimates for NGC 6302 range from ~ 0.81 kpc (Lago et al. 2019) to ~ 1.17 kpc (Meaburn et al. 2008), with a recent determination, adopted here, of 1.03 ± 0.27 kpc (Gómez-Gordillo et al. 2020). This proximity makes NGC 6302 a tempting subject for high-resolution imaging studies aimed at understanding the origin and evolution of bipolar structure in PNe. Indeed, prior to the comprehensive Cycle 27 WFC3 survey described here, NGC 6302 had already been the subject of more than two dozen HST images, including WFC3 imaging in several filters across the wavelength range 3700–6700 Å (e.g., Szyszka et al. 2009).

NGC 6302’s central pinched waist is so dusty and its bipolar symmetry axis so highly inclined (inclination of $75\text{--}78^\circ$ with respect to the line of sight; Peretto et al. 2007; Santander-García et al. 2017), that, as dryly noted by Aller et al. (1981), “[no] central star has been detected; the object definitely is not a conventional planetary nebula.” The dusty central torus harbors “mixed” (C-rich and O-rich) chemistry, displaying a combination of PAH features in the range $\sim 5\text{--}12$ μm and crystalline silicate and H_2O ice at longer IR wavelengths (Molster et al. 2001; Kemper et al. 2002). ALMA CO mapping has revealed potential connections between this dense, dusty molecular torus and the inner lobe regions near the waist of the nebula (Santander-García et al. 2017). The slowly (~ 8 km s $^{-1}$) expanding equatorial molecular torus has a dynamical age of $\sim 5000\text{--}7500$ yr (Peretto et al. 2007; Santander-García et al. 2017). In contrast, the large, open-ended bipolar lobes, which extend to ~ 1.5 pc (Kameswara Rao et al. 2018), display very high expansion velocities (~ 600 km s $^{-1}$; Meaburn et al. 2005) and, hence, appear to have been ejected more recently and over a shorter (~ 2000 yr) timescale (Meaburn et al. 2008; Szyszka et al. 2011). Again quoting Aller et al. (1981), “The nebula is clearly the result of some explosive event; its whole appearance suggests violent motions with some bilateral symmetry.”

Our new panchromatic HST/WFC3 imaging study of NGC 6302 is designed to elucidate the structure and ionization patterns of the nebula on size scales from ~ 100 au to ~ 0.5 pc, so as to constrain models of the history of its central star and the evolution of its collimated outflows. In this paper, we present the full suite of HST/WFC3 images of NGC 6302, as well as selected line ratio images, and we highlight key results gleaned from these images thus far. In forthcoming companion papers, we will provide an analogous treatment of the HST/WFC3 imaging survey of NGC 7027 (Moraga et al., in prep.), and we will present an analysis of multi-epoch HST/WFC3 imaging of NGC 6302

Table 1. HST/WFC3 IMAGING SURVEY OF NGC 6302: OBSERVATION SUMMARY

Filter	λ_0 ($\Delta\lambda$) ^a (nm)	line targeted	date	exp. (s)
FQ243N ^b	246.8 (3.6)	[Ne IV] λ 2425	2019-10-06	1110
F343N	343.5 (25.0)	[Ne V] λ 3426 ^c	2019-10-06	1110
F487N	487.1 (6.0)	H β λ 4861	2019-10-06	1200
F502N	501.0 (6.5)	[O III] $\lambda\lambda$ 4959, 5007	2020-03-13 ^d	1200
F656N	656.1 (1.8)	H α λ 6563	2019-10-06	1200
F658N	658.4 (2.8)	[N II] λ 6583	2020-03-13	2600
F673N	676.6 (11.8)	[S II] $\lambda\lambda$ 6716, 6730	2020-03-13 ^d	1290
F110W	1153.4 (443.0)	“YJ band”	2019-10-05	556
F128N	1283.2 (15.9)	Pa β 1.28 μ m	2019-10-05	506
F130N	1300.6 (15.6)	Pa β continuum	2019-10-05	506
F160W	1536.9 (268.3)	“H band”	2019-10-05	456
F164N	1640.4 (20.9)	[Fe II] 1.64 μ m	2019-10-05	1306
F167N	1664.2 (21.0)	[Fe II] continuum	2019-10-05	1306

NOTES: a) Filter pivot wavelength and bandwidth. b) Images in filter FQ243N yielded poor signal, so are not presented here. c) Contamination from continuum as well as O III λ 3444 at the \sim 10% percent level (Groves et al. 2002). d) Exposures with F502N and F673N in 2019 were unusable due to gyro lock failures.

aimed at understanding its detailed kinematics (Balick et al., in prep.). The present paper is structured as follows: we describe the HST/WFC3 observations in §2; we present the resulting image suite, and briefly describe the most notable features of the resulting image, in §3; we present and analyze line ratio images diagnostic of nebular extinction and excitation in §4; we discuss the overall structure of the nebula’s bipolar lobes, as revealed by the HST/WFC3 image and line ratio suite, in §5, while §6 consists of a discussion of what our images reveal (and can’t reveal) about the central star; finally, in §7, we present a summary and the main conclusions gleaned from this HST/WFC3 imaging study of NGC 6302.

2. OBSERVATIONS

The HST/WFC3 observations of NGC 6302 reported here were obtained during HST Cycle 27 in 2019 October and 2020 March. The UVIS (CCD) and IR (HgCdTe array) imaging modules of WFC3 provide fields of view of $\sim 2.7' \times 2.7'$ and $\sim 2.27' \times 2.27'$ at pixel scales of 0.04 arcsec/pixel and 0.13 arcsec/pixel, respectively. Table 1 provides a summary of the WFC3 filters used, lines targeted, observing dates, and exposure times. The UVIS images were obtained in 2-point GAP-LINE dither mode (DITHER-LINE for quad filter FQ243N), and the IR images were obtained in 2-point DITHERBLOB dither mode. Images obtained in 2019 October and 2020 March were obtained at orientations of -35.0° and 140.2° , respectively, as measured E of N with respect to the image Y axis.

Standard pipeline calibration and processing of the UVIS and IR exposure sets, using `CALWF3 v3.5.0`, was performed on all images¹. For both UVIS and IR imaging, the calibrations include bias correction, dark current subtraction, flat field and shutter shading corrections, and cosmic-ray rejection; pipeline UVIS image processing also includes CTE correction. Following calibration, pipeline processing² consisted of geometric distortion corrections, World Coordinate System image alignment, additional cosmic-ray rejection, and merging of dithered exposure sequences. As a result of the simple two-point dither observing mode we employed, cosmic-ray rejection was inefficient in the inter-CCD “gap” region of the UVIS module, resulting in some small-scale image artifacts along this region of the UVIS images.

We used the `AstroDrizzle` software package³ to perform an additional round of post-pipeline processing of all images, so as to (a) correct the registration of dithered exposures that were poorly aligned in standard pipeline processing (as was the case for most of the IR images), and (b) to refine relative image-to-image pointing across filters, using common field stars as the positional references. We estimate that, after this post-pipeline processing, the relative pointing across all (UVIS and IR) images is accurate to ~ 0.5 pixel. Absolute pointing was further calibrated

¹ See <https://hst-docs.stsci.edu/wfc3dhh/chapter-3-wfc3-data-calibration>

² <https://hst-docs.stsci.edu/wfc3dhh/chapter-4-wfc3-images-distortion-correction-and-astrodrizzle>

³ <https://www.stsci.edu/scientific-community/software/drizzlepac.html>

for a reference (IR) image set using reference stars from the Gaia Space Astrometry mission, by adapting standard `AstroDrizzle` scripts.

The various emission line and line ratio images presented in this paper were generated from these astrometrically calibrated images using appropriate photometric calibrations and/or passband responses, as obtained from the `synphot` software package⁴. Additional small *ad hoc* pointing refinements were performed to generate difference images from the F164N-F167N and F128N-F130N image pairs, so as to obtain continuum-subtracted $1.28\ \mu\text{m}$ $\text{Pa}\beta$ and $1.64\ \mu\text{m}$ [Fe II] images, respectively. These refinements were verified via minimization of difference image residuals in background sky regions and field star images.

3. THE HST/WFC3 IMAGE SUITE

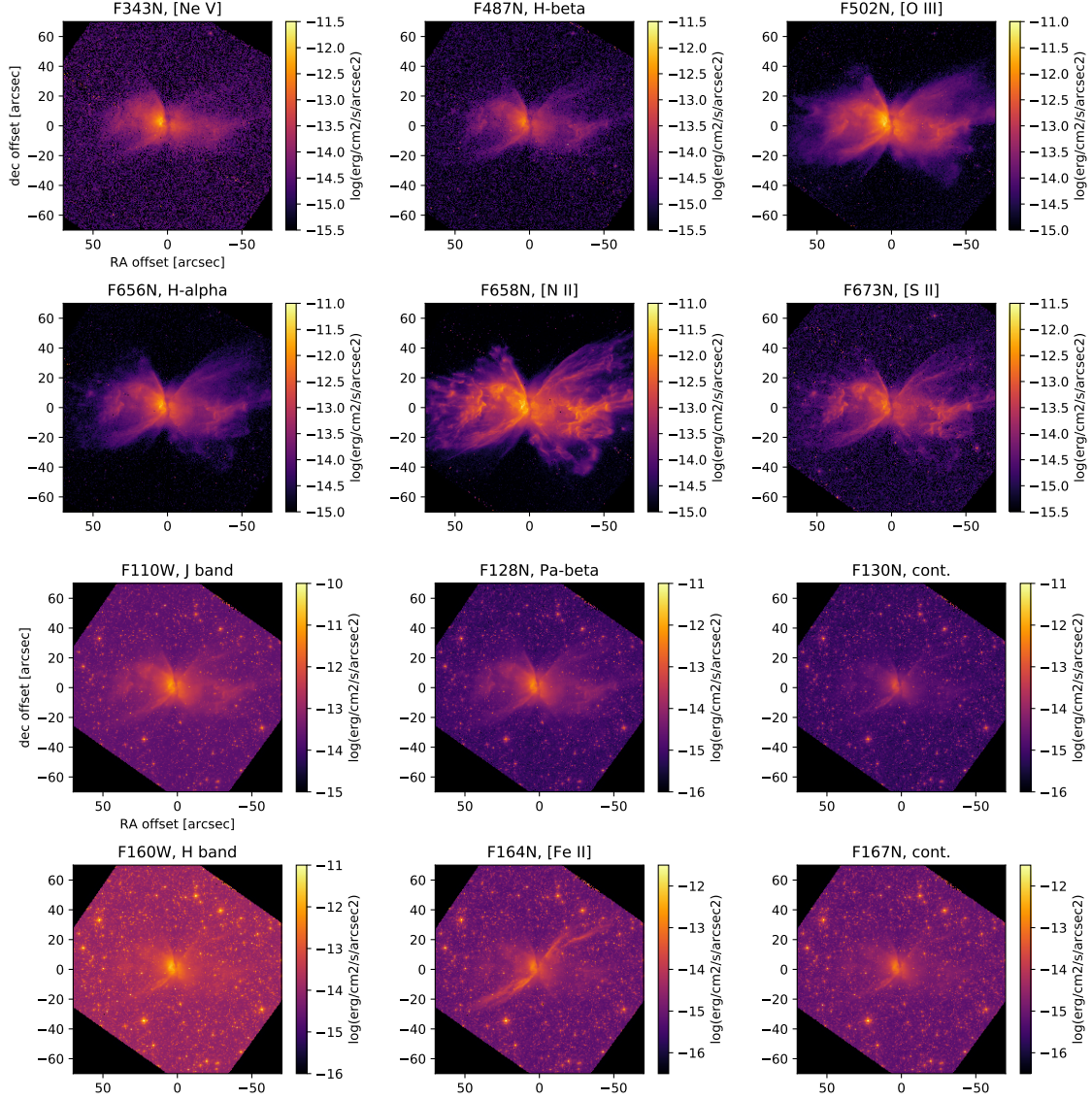


Figure 1. Suite of HST/WFC3 UVIS images obtained for NGC 6302. Field of view is $140'' \times 140''$; N is up and E is to the left.

⁴ <https://www.stsci.edu/hst/instrumentation/reference-data-for-calibration-and-tools/synphot-throughput-tables.html>

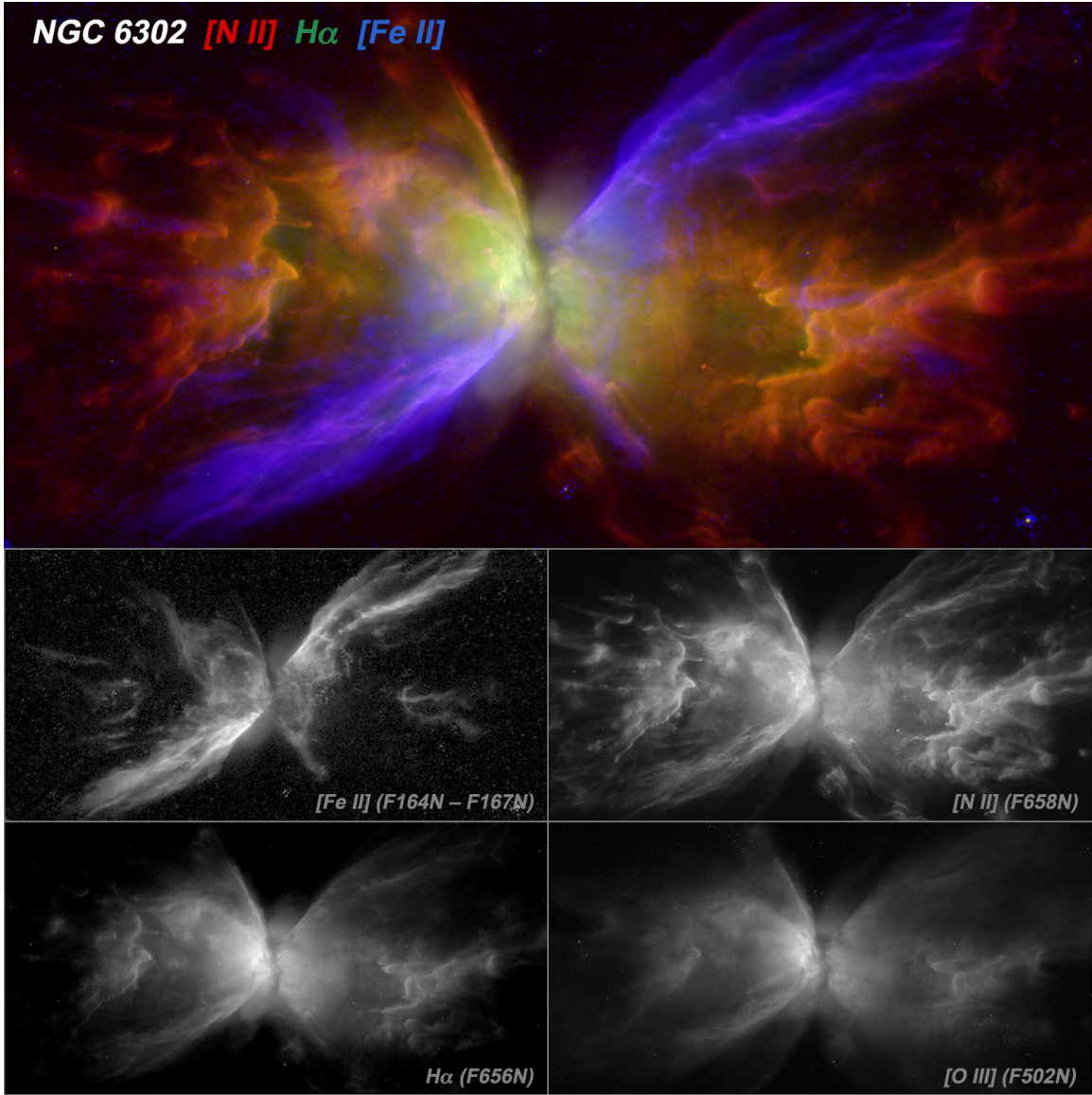


Figure 2. Color overlay of WFC3 narrowband images of NGC 6302, with [Fe II] (F164N–F167N difference image) coded blue, H α (F656N) coded green, and [N II] (F658N) coded red. The three component images, along with the [O III] (F502N) image, are displayed in greyscale in the lower panel. Field of view is $130'' \times 64''$; N is up and E is to the left.

The suite of HST/WFC3 images obtained for NGC 6302 is presented in Fig. 1. Across this WFC3 image suite, as in the (WFPC2 and WFC3) images previously obtained by HST (Matsuura et al. 2005; Szyszka et al. 2009, 2011), NGC 6302 displays its classical, pinched-waist bipolar morphology, with its lobe-bisecting dark lane (the projection of its dusty torus against the sky) oriented very nearly N–S (see also Kameswara Rao et al. 2018). The new WFC3 image suite clearly defines the wavelength-dependent morphologies of the dusty toroidal equatorial structure (central dark lane) that bisects the polar lobes, as well as the fine structures (clumps, knots, and filaments) within the lobes. On large (~ 60 – $90''$; ~ 0.3 – 0.45 pc) scales, the two large, “major” lobes are oriented more or less E–W, i.e., orthogonally to the dusty equatorial torus. However, it also evident that the lobes contain a complex system of point-symmetric sets of knot and filament structures spanning a broad ranges in both size scale and position angle (i.e., PAs from $\sim 20^\circ$ to $\sim 150^\circ$), and that the relative strengths of these lobe features vary sharply with wavelength and from emission line to emission line.

Undoubtedly the most striking and unexpected aspect of the new WFC3 image suite is the bright, S-shaped $1.64 \mu\text{m}$ [Fe II] emission that traces the southern interior of the east lobe rim and the northern interior of the west lobe

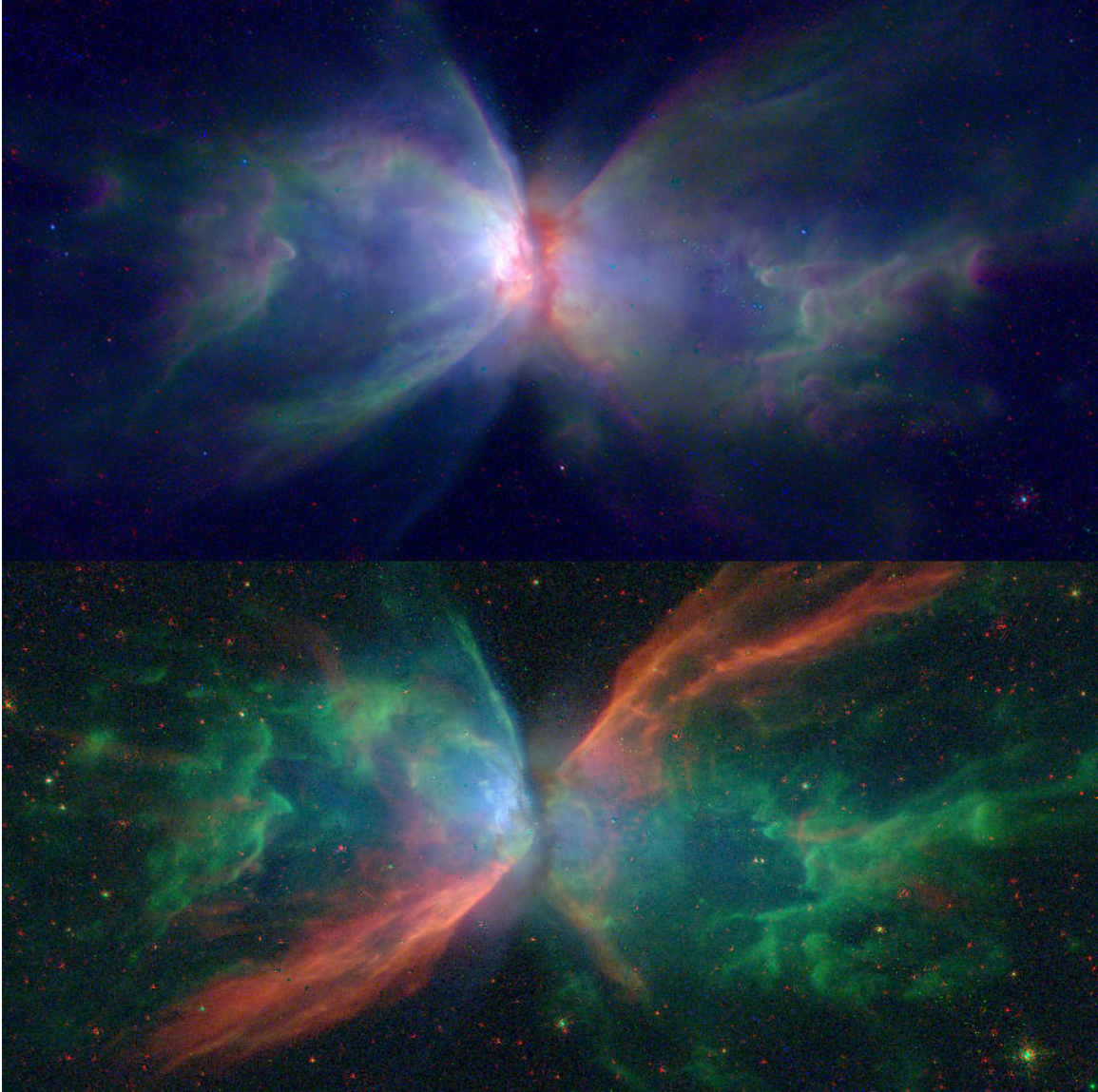


Figure 3. Color overlays of WFC3 narrowband images of NGC 6302. Top: overlay with Pa β (F128N–F130N difference image) coded red, [O III] (F502N) coded green, and [Ne v] (F343N) coded blue. Fields of view are $130'' \times 64''$; N is up and E is to the left. Bottom: overlay with [Fe II] (F164N–F167N difference image) coded red, [S II] (F673N) coded green, and [Ne v] (F343N) coded blue.

rim, in point-symmetric fashion (Fig. 2). Fainter [Fe II] emission is also detected in the lobe interiors, especially to the northeast of the dark lane, as well as in the lobe “clump zones” (§ 5.1). This constitutes the first detection of $1.64 \mu\text{m}$ [Fe II] emission in NGC 6302; although the line is evidently very bright (peak surface brightness $\sim 3 \times 10^{-14} \text{ erg cm}^{-2} \text{ s}^{-1} \text{ ster}^{-1}$), previous near-IR spectroscopy of NGC 6302 had not covered this (H band) spectral region (Ashley & Hyland 1988; Casassus et al. 2000, 2002). The presence and morphology of $1.64 \mu\text{m}$ [Fe II] emission is indicative of the presence of off-axis shocks generated by fast ($\gtrsim 100 \text{ km s}^{-1}$), collimated winds from the central star(s) of NGC 6302, as is discussed in detail in later sections of this paper.

It is furthermore readily evident that the surface brightnesses of the high-excitation species [Ne v] and [O III] and the H recombination lines (H β , H α , Pa α) fall off more steeply with increasing displacement from the pinched waist than those of [N II] and [S II], with the latter, lower-excitation lines conspicuously bright in the nebula’s clump and knot structures and remaining bright out to large displacements ($>2'$, i.e., $>0.6 \text{ pc}$) in the polar lobes. These gradients in nebular ionization and excitation are illustrated in the form of RGB image overlays in Fig. 3, and are even more apparent in the line ratio images presented in §4.2. The top panel of this Figure shows that [Ne v] emission appears

somewhat more compact than [O III], with the caveat that the F343N [Ne v] filter is more susceptible than F502N [O III] to contamination by scattered starlight in the dusty lobe interiors. This color overlay also reveals small-scale excitation gradients in the clump regions of the lobes (which are discussed in more detail in §5.1), illustrating in particular how the [O III] follows the clump exteriors, while Pa α emission effectively traces ionized regions that are highly dust-extincted. The bottom frame of Fig. 3 furthermore demonstrates the dramatically different extents of [Ne v] vs. [S II] emission and the strikingly different morphologies of [S II] and [Fe II].

4. LINE RATIO IMAGES

4.1. *H* recombination lines: mapping extinction

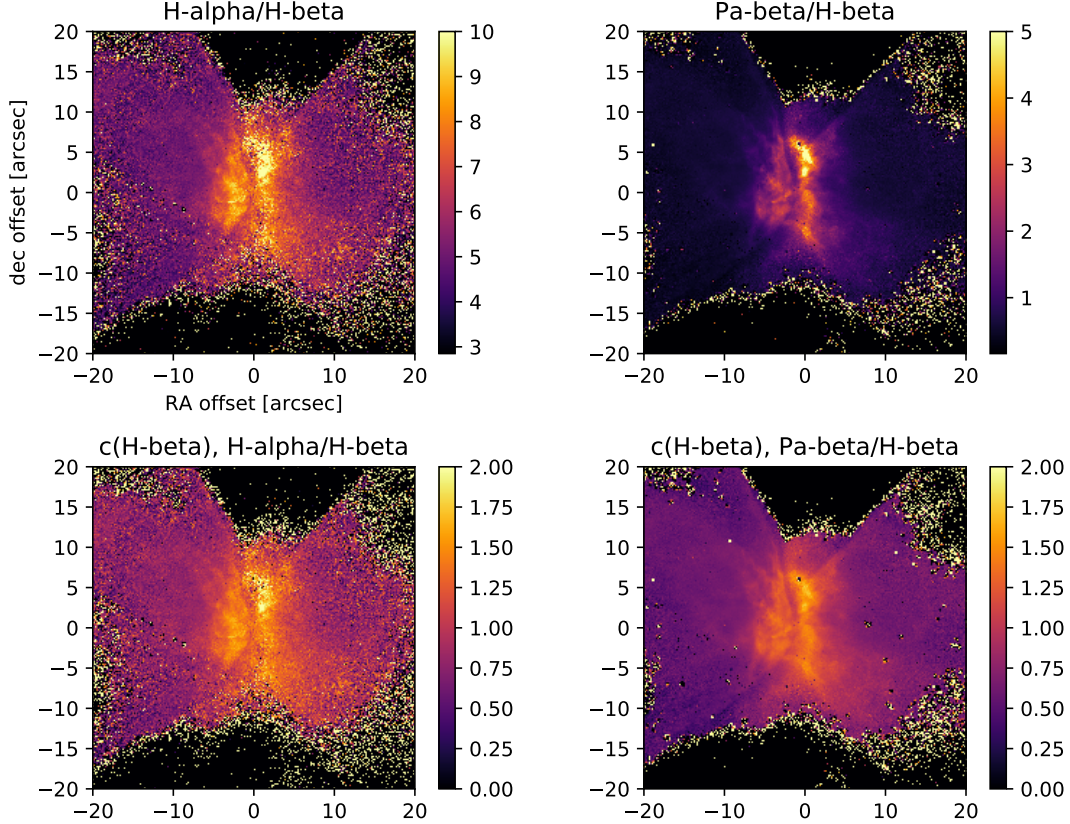


Figure 4. Top row: $H\alpha/H\beta$ (left) and $Pa\beta/H\beta$ (right) line ratio images of NGC 6302. Bottom row: maps of H I line decrement extinction parameter (c) constructed from $H\alpha/H\beta$ (left) and $Pa\beta/H\beta$ (right) line ratio images. Field of view is $40'' \times 40''$; N is up and E is to the left.

In Fig. 4 (top panels), we present H recombination line ratio images ($H\alpha/H\beta$ and $Pa\beta/H\beta$) of the central $40'' \times 40''$ region of NGC 6302. In the regimes of electron temperature and density appropriate to NGC 6302 (i.e., $\sim 1.5 \times 10^4$ K and $\sim 10^4$ cm $^{-3}$, respectively; Rauber et al. 2014), the theoretical (Case B) line ratios are $H\alpha/H\beta \sim 2.85$ and $Pa\beta/H\beta \sim 0.162$ (Osterbrock & Ferland 2006). It is readily apparent from Fig. 4 that the observed ratios in NGC 6302 are everywhere larger than the theoretical ratios, by factors ranging from ~ 2 in the lobes to as large as ~ 30 , in the case of $Pa\beta/H\beta$ in the central torus (dark lane) region. These large deviations are caused by reddening that, in turn, is due to a combination of foreground (ISM) and intranebulary dust extinction. Whereas ISM reddening (estimated at $E(B - V) \approx 0.3$ toward NGC 6302; Lallement et al. 2019) likely dominates the (relatively smooth) extinction toward the lobe regions, intranebulary extinction clearly becomes the dominant extinction source in the central torus region (similar conclusions were reached in previous studies of NGC 6302; e.g., Matsuura et al. 2005; Rauber et al. 2014). This contrast is perhaps best seen in the $Pa\beta/H\beta$ image; the factor ~ 3 wavelength range spanned by this ratio makes it a sensitive probe of the highly reddened central regions of NGC 6302.

Maps of the nebular extinction parameter c obtained from the $H\alpha/H\beta$ and $Pa\beta/H\beta$ line ratio images are presented in the bottom panels of Fig. 4. These maps were generated from the relation $c = [\log(R_c/R_o)]/[f(\lambda_2) - f(\lambda_1)]$ (e.g., Groves et al. 2002), where R_c and R_o are the theoretical and observed line ratios and $f(\lambda_1)$, $f(\lambda_2)$ are extinction values at the relevant wavelengths as given by a reddening law. Here, we adopted the ISM reddening law determined by Cardelli et al. (1989).

The detailed morphologies of the resulting c maps in Fig. 4 are fully consistent. However, the values of c in the map derived from $Pa\beta/H\beta$ are systematically smaller than those derived from $H\alpha/H\beta$; the map obtained from $Pa\beta/H\beta$ ranges from $c \sim 0.6$ (lobes) to a peak of $c \sim 1.7$ within the central waist region, compared with the corresponding range of $c \sim 0.8$ – 2.0 for the map obtained from $H\alpha/H\beta$. This discrepancy may reflect deviations from “standard” ISM dust extinction behavior as encoded in the reddening law from Cardelli et al. (1989).

We note that the ranges of c we derive from our HST/WFC3 H recombination line ratio images (Fig. 4) are in reasonable agreement with previous determinations for c in NGC 6302 as obtained from long-slit spectroscopy, aperture spectroscopy, and/or aperture photometry at wavelengths ranging from the visible to the radio, i.e., $c \sim 0.8$ in the lobes and $c \sim 1.2$ to ~ 2.4 in the central torus region (Groves et al. 2002; Rauber et al. 2014, and references therein). At the same time it is readily apparent, given the very large range in c observed in our extinction maps, that previous measurements would be tremendously sensitive to the specifics of aperture placement, wavelength span, and assumed reddening law. This of course has profound implications for determinations of line ratios and (hence) ionic abundances, temperatures, and densities within the nebula (see also Rauber et al. 2014).

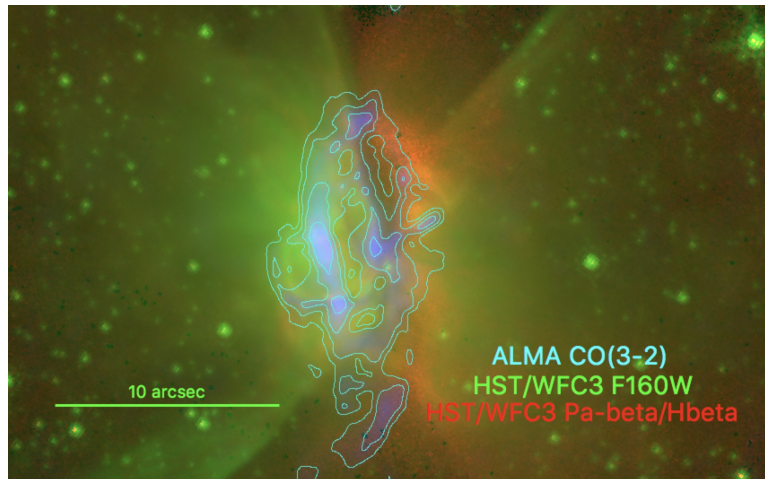


Figure 5. Color overlay of ALMA map of 345 GHz CO $J = 3 \rightarrow 2$ emission (blue and contours) from Santander-García et al. (2017) on HST/WFC3 $Pa\beta/H\beta$ line ratio and F160W (“H band”) images (red and green, respectively). The $Pa\beta/H\beta$ ratio image is displayed on a square-root intensity scale, with a range of 0.16–6.8. The CO contour levels are 0.025, 0.4, 0.8, 1.5, and 2.5 Jy km s $^{-1}$ beam $^{-1}$, and the beamsize is 0.36″. Field of view is 35″ \times 20″; N is up and E is to the left.

In Fig. 5 we present a color overlay of the ALMA integrated intensity map of 345 GHz CO $J = 3 \rightarrow 2$ emission from Santander-García et al. (2017) on our HST/WFC3 $Pa\beta/H\beta$ line ratio and F160W (“H band”) images, zoomed in on the core region of the nebula. As described in detail in Santander-García et al. (2017), the main bright loop of CO traces the molecular gas within the central, expanding, dusty torus that obscures the CSPN of NGC 6302. While the overall correspondence between the surface brightness of CO emission and the distribution of dust extinction (as mapped by $Pa\beta/H\beta$) is apparent in Fig. 5, the CO and dust extinction morphologies clearly differ in detail. In particular, the western rim of the CO loop, which is blueshifted (Santander-García et al. 2017), precisely traces the sharp, narrow minimum in $Pa\beta/H\beta$ that bisects this line ratio image. This spatial correspondence between blueshifted CO and the $Pa\beta/H\beta$ “dark lane” indicates that the forward-facing portion of the expanding CO loop traces a large intervening column of dust — a dust column large enough that too few $Pa\beta$ line photons escape for the $Pa\beta/H\beta$ ratio to serve as a probe of the dust extinction. The fact that the $Pa\beta/H\beta$ ratio rises to its maximum value (~ 2.0) at a displacement $\sim 2''$ west of this sharp minimum, before declining (a result generally consistent with that from long-slit optical spectral mapping; Rauber et al. 2014), then reveals the radial extent of the dusty torus as seen in projection toward the west lobe, i.e., ~ 2000 au. In contrast, the bright eastern rim of the CO loop, which is redshifted (Santander-García et al.

2017), has no clear counterpart in the $\text{Pa}\beta/\text{H}\beta$ line ratio image. This portion of the central molecular torus is projected behind the east lobe, such that its dust counterpart cannot be traced via extinction mapping.

4.2. High- and low-excitation forbidden lines: ionization gradients

In Fig. 6, we present a series of line ratio images obtained from high-excitation forbidden lines ($[\text{Ne v}]$, $[\text{O III}]$) and low-excitation forbidden lines ($[\text{S II}]$, $[\text{N II}]$) with respect to each other and to H recombination lines. Of these line ratio images, only $[\text{O III}]/[\text{Ne v}]$ should be sensitive to extinction. Given the results above (§ 4.1), however, this ratio should only be affected by extinction within the central torus region, where contamination of the F343N $[\text{Ne v}]$ image by continuum and O III Bowen fluorescence line emission is also likely most significant (see Groves et al. 2002, their Fig. 2). We note that the (relatively broad) F343N is the only UVIS filter that should be affected by such contamination due to continuum or line emission.

The $[\text{O III}]/\text{H}\beta$, $[\text{S II}]/\text{H}\alpha$, and $[\text{N II}]/\text{H}\alpha$ line ratio images, along with $\text{Pa}\beta/\text{H}\beta$ and $[\text{Fe II}]$ images (as nebular extinction and shock tracers, respectively; see § 4.1 and below), are also presented in the form of color overlays in Fig. 7. In Fig. 8, we display profiles of the values of the $[\text{O III}]/\text{H}\beta$, $[\text{S II}]/\text{H}\alpha$, and $[\text{N II}]/\text{H}\alpha$ line ratios as measured along (three) selected linear cuts through the line ratio images — one cut along the E-W direction through the inferred position of the central star (see § 6), and two N-S cuts through the inner lobe regions — with the positions and lengths of these cuts indicated in the color overlays at the top of the Figure.

Broadly speaking, the ionization structure observed in these HST/WFC3 line ratio maps — wherein the higher ionization state species (Ne^{4+} , O^{2+}) are brightest in the lobe interiors, and the lower ionization species (singly ionized S and N) become most prominent in the outer reaches of the nebula, relative to $\text{H}\beta$ and $\text{H}\alpha$ (respectively) — is consistent with the predictions of (e.g., CLOUDY) models of planetary nebulae with simple (spherical) geometries that are photoionized by hot central stars (e.g., Alexander & Balick 1997). This ionization structure is readily apparent in Fig. 7, upper panel, and in the E-W cut through the polar lobes displayed in Fig. 8. However — even accounting for the likely additional contribution of shocks (Lago et al. 2019) — the line ratio images clearly deviate from such simple prescriptions in fundamental respects, which we highlight here.

The most striking aspect of the line ratio images involving the high-excitation lines is the series of radially directed, azimuthally alternating high/low ratio features, extending away from the central waist region. These features are most noticeable within the east lobe, where they more or less coincide with the boundaries of the distinct azimuthal regions (wedges) discussed in detail in Sec. 5. The $[\text{O III}]/\text{H}\beta$ ratio lies in the range ~ 10 – 15 across much of the lobe regions (Fig. 8), consistent with previous spectroscopic mapping within a $\sim 200'' \times 10''$ strip oriented along the polar axis of NGC 6302 by Rauber et al. (2014), and as expected for high-excitation nebulae (e.g., Alexander & Balick 1997). However, the $[\text{O III}]/\text{H}\beta$ ratio is observed to climb to ~ 15 – 20 in narrow strips oriented along PAs $\sim 60^\circ$ and $\sim 120^\circ$, and drops to distinct minima of $[\text{O III}]/\text{H}\beta \sim 6$ – 8 along PAs $\sim 20^\circ$, $\sim 45^\circ$, and $\sim 150^\circ$. These strips of elevated and depressed $[\text{O III}]/\text{H}\beta$ ratio can be seen as peaks and valleys in the N-S cut through the east lobe displayed in Fig. 8. Radially aligned (azimuthally alternating) features of locally high and low $[\text{O III}]/\text{H}\beta$ ratio are also seen in the west lobe, but are generally less distinct, with the exception of narrow radial strips of low $[\text{O III}]/\text{H}\beta$ (~ 5) along the lobe perimeters (PAs $\sim 200^\circ$ and $\sim 315^\circ$). The N-S profiles displayed in Fig. 8 (lower panels) furthermore demonstrate that the minima in $[\text{O III}]/\text{H}\beta$ along the southern and northern perimeters of the east and west lobes, respectively, correspond to sharp peaks in $[\text{Fe II}]$ surface brightness.

The $[\text{O III}]/[\text{Ne v}]$ ratio image morphology closely follows that of $[\text{O III}]/\text{H}\beta$, wherein $[\text{O III}]/[\text{Ne v}]$ is somewhat elevated within the radial features that display larger $[\text{O III}]/\text{H}\beta$. Since the ionization potential of Ne^{3+} is much larger than that of O^+ (97 eV vs. 35 eV), this suggests that the azimuthal regions characterized by low $[\text{O III}]/\text{H}\beta$ and $[\text{O III}]/[\text{Ne v}]$ are in fact the highest-excitation regions of the nebula; i.e., in these regions, where $[\text{Ne v}]$ is bright but $[\text{O III}]$ is relatively weak, O^{2+} is suppressed in favor of higher ionization states of O. The implied large azimuthal ionization gradients are impossible to reconcile with standard (Strömgren-sphere-based) ionization theory, and point instead to shadowing effects. That is, the lobe regions with suppressed $[\text{O III}]/\text{H}\beta$ and $[\text{O III}]/[\text{Ne v}]$ are likely directly exposed to EUV and soft X-ray radiation from NGC 6302’s exceedingly hot central star; whereas the radial zones of elevated $[\text{O III}]/\text{H}\beta$ and $[\text{O III}]/[\text{Ne v}]$ mark regions where radiation from the central star is at least partially attenuated, perhaps by intervening dust.

The structures observed in the line ratio images constructed from $[\text{N II}]$ and $[\text{S II}]$ differ fundamentally from those of the high-excitation forbidden lines. In particular, as is evident from the profiles displayed in Fig. 8, these low-excitation lines are particularly bright (with respect to $\text{H}\alpha$) in the clump and “elephant trunk” structures within the lobe interiors

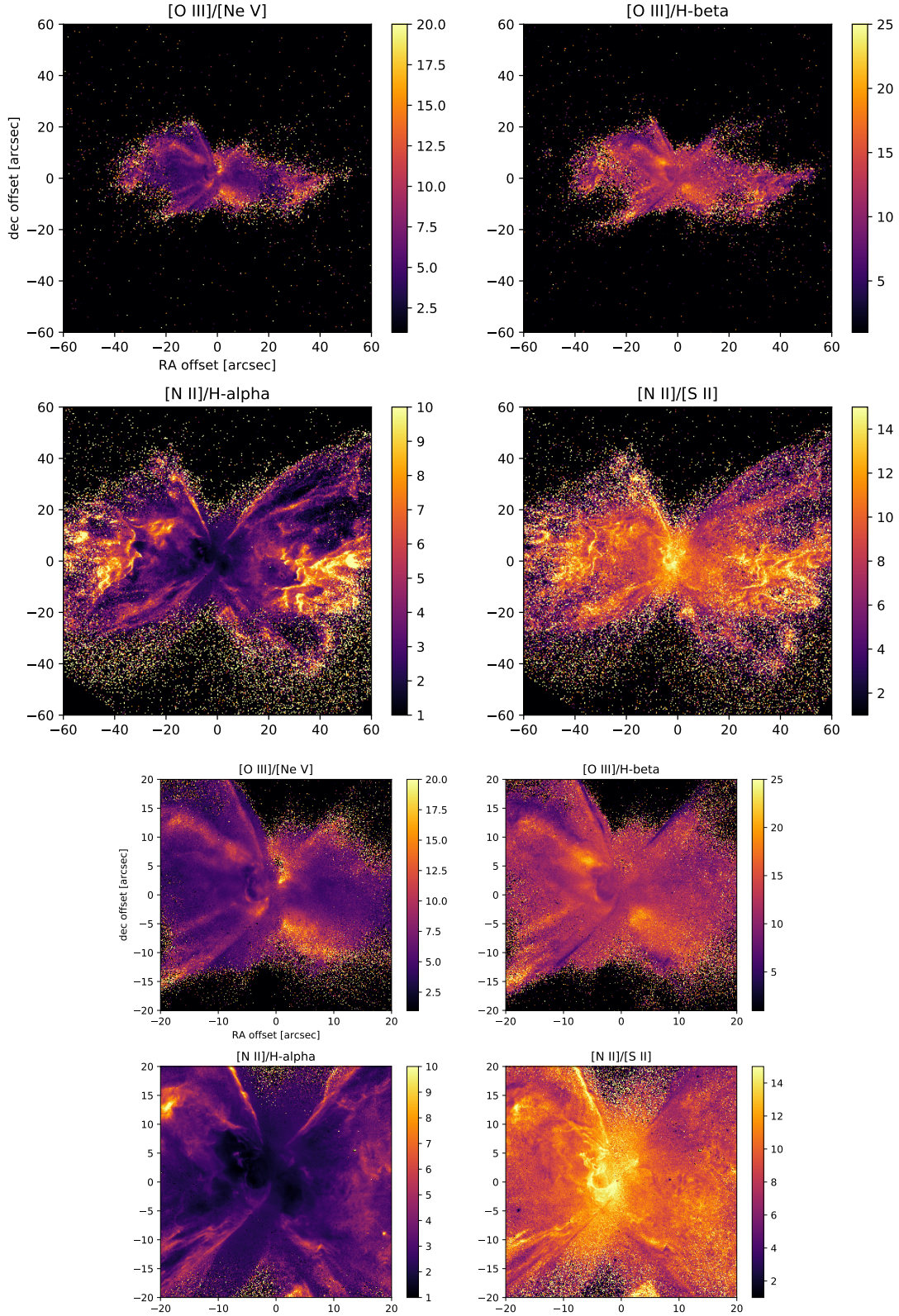


Figure 6. Various line ratio images of NGC 6302. In each set of four panels, $[\text{O III}]/[\text{Ne V}]$ (F502N/F343N; left) and $[\text{O III}]/\text{H}\beta$ (F502N/F487N; right) are displayed in the top row, and $[\text{N II}]/\text{H}\alpha$ (F658N/F656N; left) and $[\text{N II}]/[\text{S II}]$ (F658N/F673N; right) are displayed in the bottom row. Fields of view are $120'' \times 120''$ (top panels) and $40'' \times 40''$ (bottom panels); N is up and E is to the left.

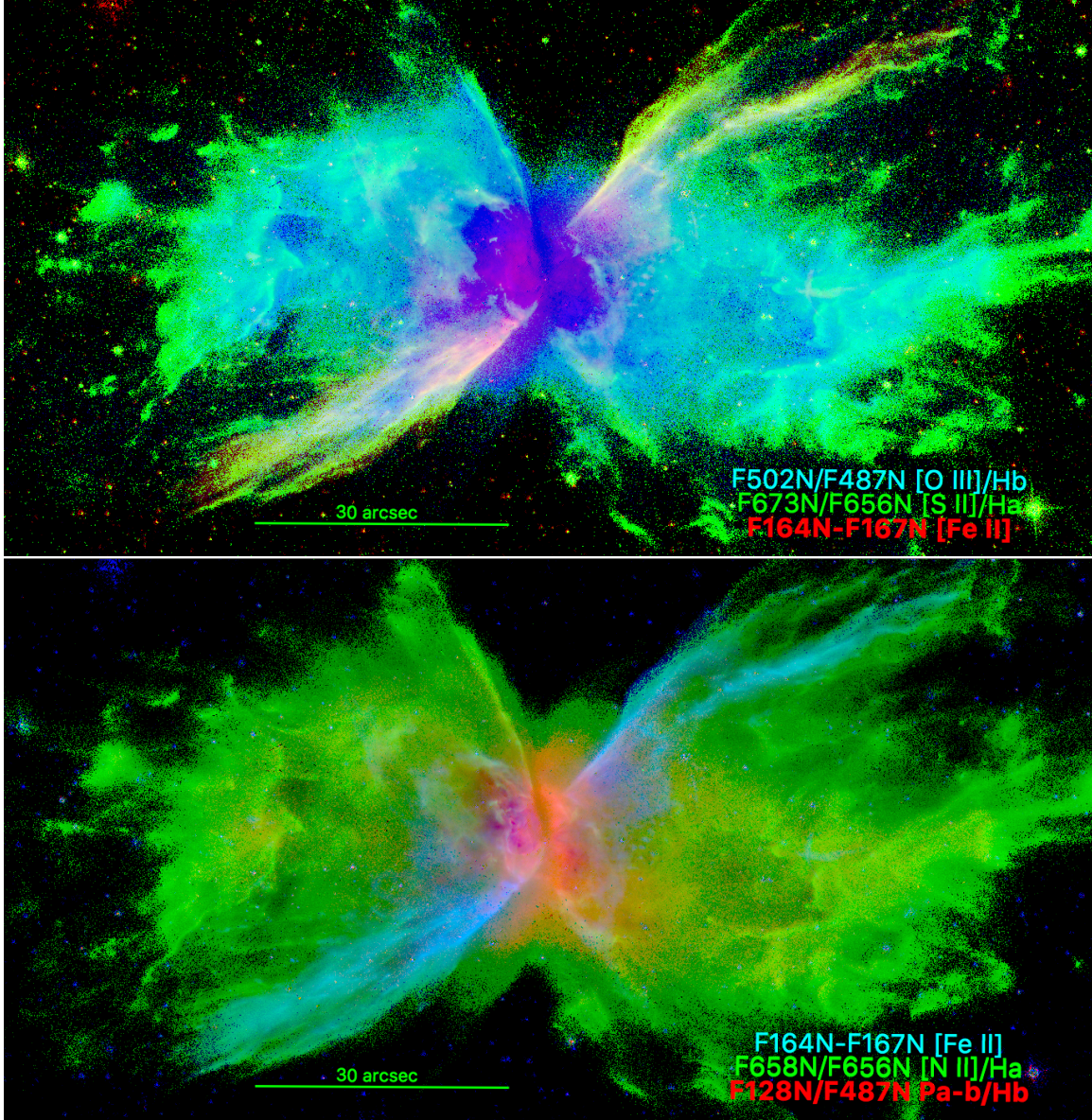


Figure 7. Color overlays of WFC3 line ratio and 1.64 μm [Fe II] images of NGC 6302, rendered in log scale. Top: [O III]/H β (F502N/F487N; range 1.0–30), [S II]/H α (F673N/F656N; range 0.2–1.0), and [Fe II] (F164N–F167N difference image) coded blue, green, and red, respectively. Bottom: [Fe II], [N II]/H α (F658N/F656N; range 1.0–30), and Pa β /H β (F128N–F130N divided by F487N; range 0.5–5.0) coded blue, green, and red, respectively. Field of view is $120'' \times 70''$; N is up and E is to the left.

at offsets of $\sim 30''$ – $60''$ from the core region. These regions are discussed in detail in § 5.1. In the core region, we find [N II]/H $\alpha < 3$, whereas within the clump regions of the lobe interiors, the [N II]/H α ratios climb to ~ 10 . The lobe perimeters, which are marked by very sharp gradients in [O III]/H β ratio, appear as narrow regions of enhanced [N II]/H α and [S II]/H α . The profiles in Fig. 8 also demonstrate that the [N II]/[S II] line ratio is ~ 10 throughout much of the nebula, with the exception of the core region and the west lobe clumps and perimeter regions. The core region is both deficient in low-excitation forbidden line emission and relatively high in [N II]/[S II] line ratio ([N II]/[S II] ~ 15). The clumps and perimeter regions in the west lobe also display [N II]/[S II] ratios of ~ 15 – 20 . As is the case for [O III]/H β , these [N II]/H α and [S II]/H α (hence [N II]/[S II]) line ratio mapping results are quite consistent with those presented in Rauber et al. (2014), but obviously our images expand the line ratio coverage to the entire surface area of both lobes, and at subarcsecond resolution.

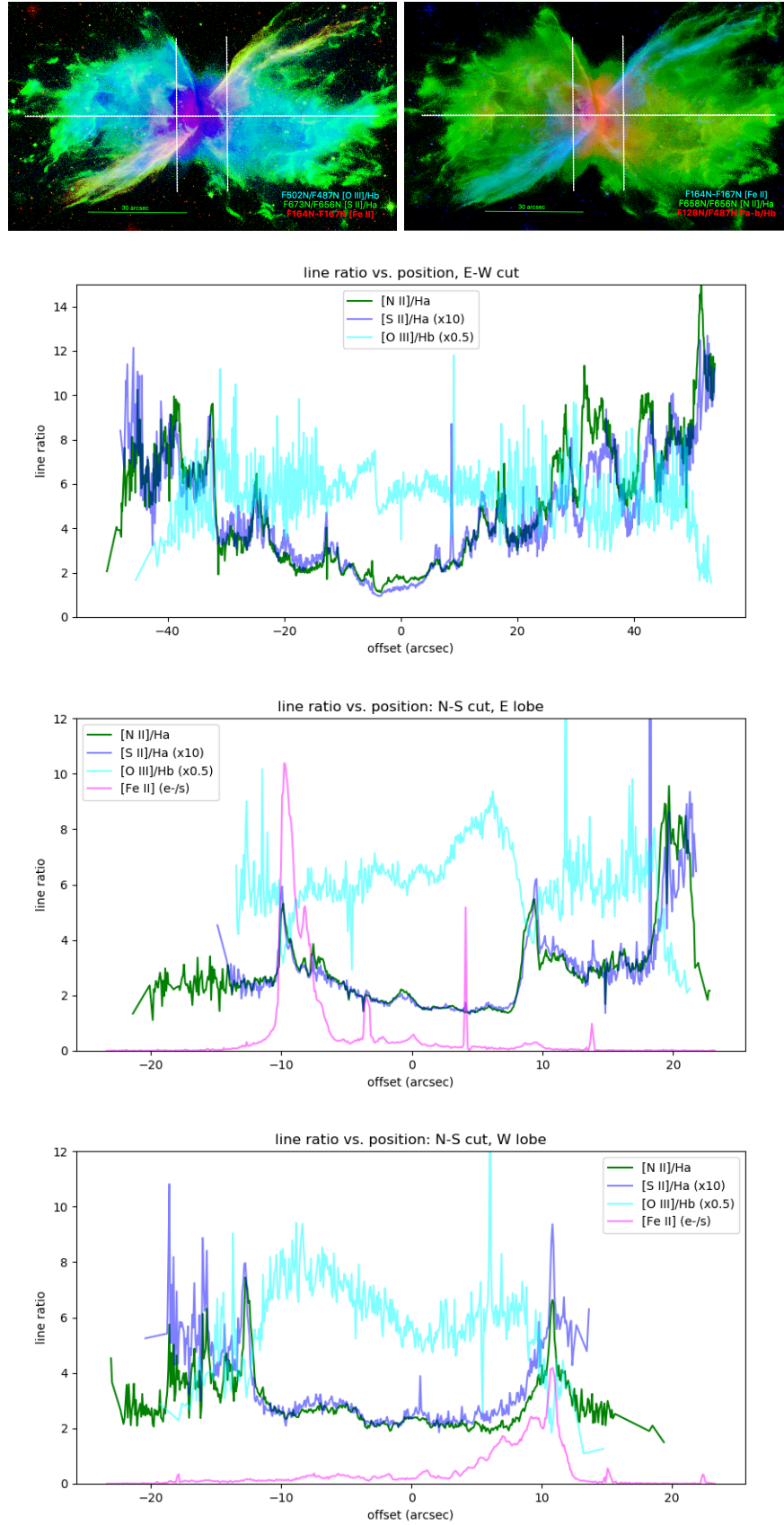


Figure 8. Top panels: Color overlays of WFC3 line ratio and 1.64 μm [Fe II] images of NGC 6302, from Fig. 7, overlaid with white lines indicating the positions (lengths and orientations) of the ($2''$ wide) apertures used to extract the spatial line ratio profiles displayed in the next three panels. Middle upper panel: E-W cut through the inferred position of the central star (see § 6), with positive (negative) indicating offset W (E) of this position. Middle lower panel: N-S cut through the E lobe. Bottom panel: N-S cut through the W lobe.

As discussed in detail in [Lago et al. \(2019\)](#), the unusually large $[\text{N II}]/\text{H}\alpha$ ratios of ~ 10 measured in the lobe clump regions are indicative of the influence of shocks on the observed ionization structure of NGC 6302. Indeed, there is ample evidence for the presence of relatively strong ($\gtrsim 100 \text{ km s}^{-1}$) shocks in NGC 6302, both on the basis of large- and small-scale nebular morphology and in the form of the bright $1.64 \mu\text{m}$ $[\text{Fe II}]$ emission discovered in our HST/WFC3 imaging (both aspects are discussed further in Sec. 5). Such fast shocks might explain the large observed $[\text{N II}]/\text{H}\alpha$ in the clumps as well as the elevated $[\text{N II}]/[\text{S II}]$ ratios in both the clump and core regions, according to models describing Herbig-Haro objects associated with collimated outflows from pre-main sequence stars ([Hartigan et al. 1994](#)) — assuming such models might be applicable to the extreme UV irradiation environment that characterizes NGC 6302. However, the widely distributed lobe clump regions, where the most highly elevated $[\text{N II}]/\text{H}\alpha$ ratios are observed, do not spatially coincide with the (narrow) zones of bright $1.64 \mu\text{m}$ $[\text{Fe II}]$ emission (Fig. 7, lower panel). Furthermore, models specifically formulated to describe shocked “cloudlets” in planetary nebulae do not achieve such large $[\text{N II}]/\text{H}\alpha$ ratios, although these models can reproduce the $[\text{N II}]/[\text{S II}]$ ratios we measure in the clump and core regions of NGC 6302 ([Raga et al. 2008](#)).

5. THE AZIMUTHAL LOBE STRUCTURES OF NGC 6302

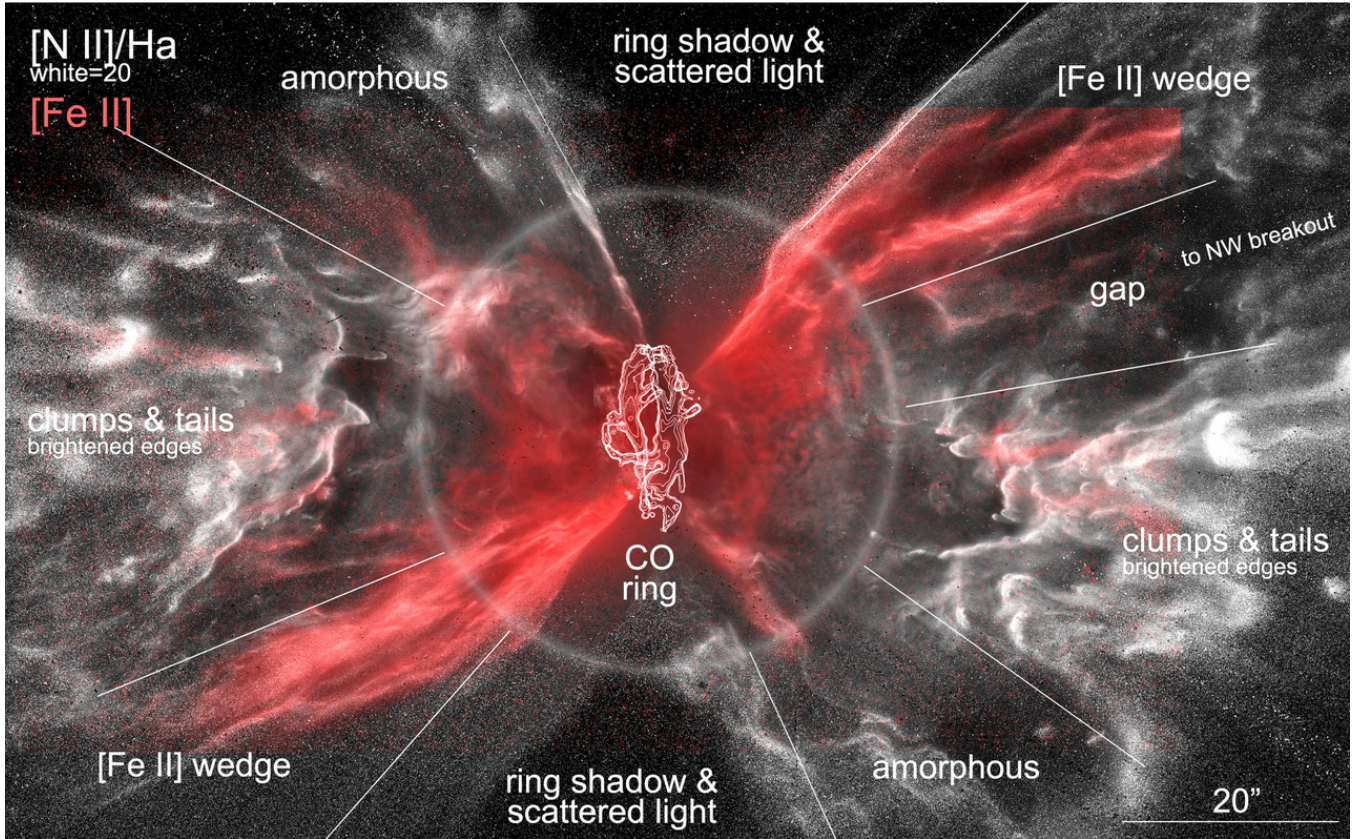


Figure 9. Overlay of $[\text{O III}]/\text{H}\beta$ ratio image (greyscale) and $[\text{Fe II}]$ image (red), annotated to indicate the various azimuthally organized zones (wedges) of NGC 6302 that are described in the text (§ 5). Contours of the ALMA map of CO emission from the central torus region ([Santander-García et al. 2017](#)) are overlaid in white. The $\sim 20''$ radius white circle delineates the approximate extent of the nebular core region.

As illustrated in Fig. 9, the regions beyond the central nebular core region of NGC6302 (whose extent is roughly delineated by the white circle in the Figure) can be divided into distinct azimuthal wedges that extend radially outward from the core. As noted in § 4.2, the boundaries of these wedge-shaped regions (indicated in Fig. 9 as thin white lines extending radially away from the core region) are marked by strong azimuthal gradients in nebular ionization structure. Such a clear azimuthal segmentation of spatial structure and ionization in the lobe interiors is highly unusual in bipolar PNe, apart from certain multipolar PNe.

The general structure of the azimuthal lobe domains is as follows. Nearest the E-W nebular symmetry axis lie oppositely positioned wedge regions containing highly conspicuous clumps with radially-directed outward-pointing tails. Moving clockwise, we find opposing wedges, marked “amorphous” in Fig. 9, that display a paucity of structure relative to the adjacent E-W oriented clump zones. The next wedges, marked “ring shadow & scattered light,” are dark. These wedges mark azimuthal angles where the central dusty, equatorial torus evidently obscures the central star from the standpoint of any nebular material that may be present beyond a few arcsec from the central waist. This dark shadow zone is bordered by (what appears to be) faint dust-scattered scattered nebular emission. Continuing clockwise, the wedges containing the plumes of [Fe II] are found next. An additional wedge at PA $\sim -60^\circ$ appears as a gap, and marks the inner regions of a pc-scale “breakout” lobe to the west, i.e., a region of the W lobe in which both the proper motions and the Doppler speed of lobe widening are extreme (e.g., Meaburn et al. 2005, 2008). (The breakout lobe will be explored in a second paper on nebular dynamics.)

5.1. The “clump” wedges

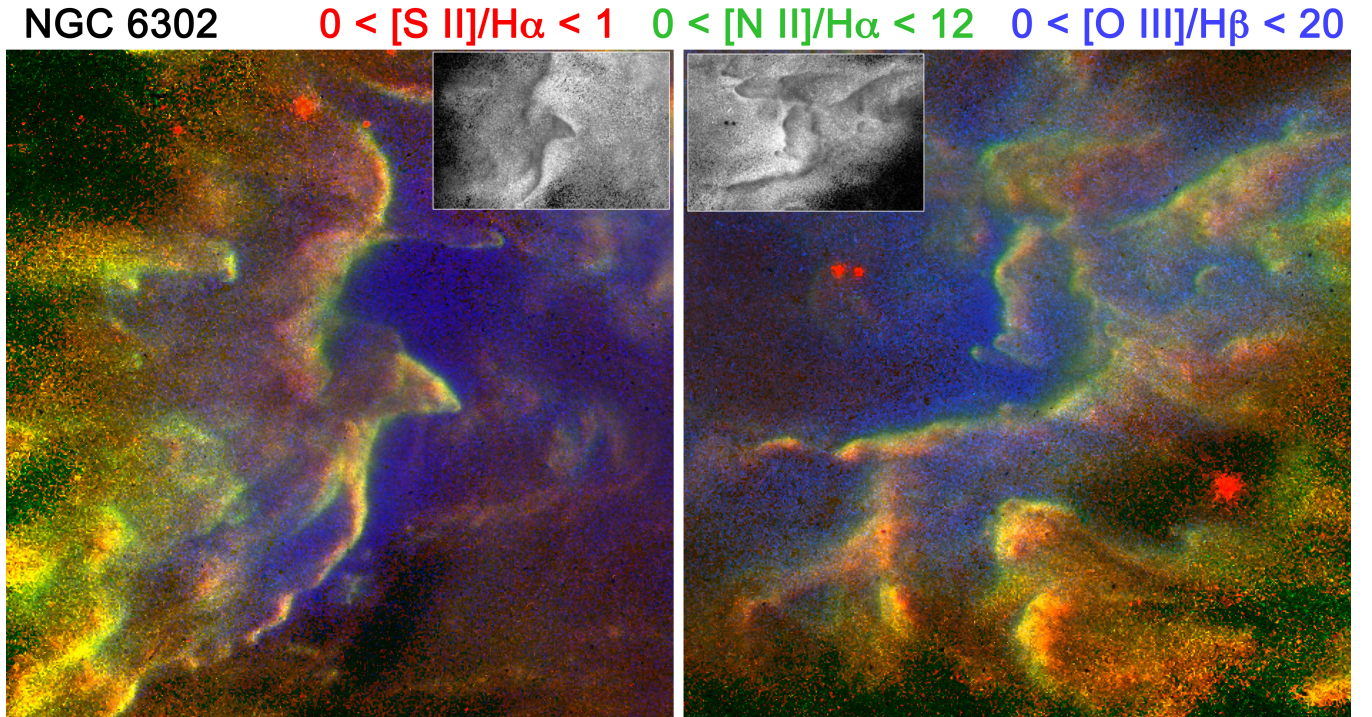


Figure 10. Color overlays of WFC3 line ratio images within $25'' \times 25''$ regions of NGC 6302 centered on the east (left) and west (right) clump zones. In the two panels, [O III]/H β (F502N/F487N), [N II]/H α (F658N/F656N), and [S II]/H α (F673N/F656N) are coded blue, green, and red, respectively. The insets show greyscale representations of the central $20'' \times 15''$ regions of the [O III]/H β ratio image.

Figure 10 illustrates the ionization structure and selected line ratios for the E-W oriented “clump” wedges of the nebula, via blowups of the brightest clump regions, exploiting line ratios that are relatively insensitive to extinction. The line ratios are sensitive to both the degree of ionization and the local excitation temperature. The lobe clumps stand out in [N II]/H α and (to a lesser extent) [S II]/H α (yellow-green regions in color panels of Fig. 9) and are notably darkened in [O III]/H β (Fig. 9, see greyscale insets). The ratios of the optical forbidden lines to neighboring Balmer lines (at adjacent wavelengths) are all enhanced on the star-facing edges of the clumps, much like the clumps at the perimeters of most photoionized H II regions and some wind-shocked clumps seen in H-H objects (Hartigan et al. 1994).

The “leeward” sides of the clumps (i.e., the sides facing away from the CSPN) uniformly display tails, with widths similar to the clump diameters, pointing away from the central star. These structures resemble (at least superficially) the dense, tail-bearing globules seen in dusty, molecule-rich PNe like NGC 6720 (the Ring; Speck et al. 2003) and NGC 7293 (the Helix; O’dell & Handron 1996). As in those PNe, the clump tails in NGC 6302 suggest that radially directed

CSPN winds with significant ram pressure are sweeping clump material outwards. That is, the tails resemble wakes that trail the clumps at their heads, indicating that they are immersed and entrained in a wind whose speed mildly exceeds the speed of the shock that strikes the heads. The fact that some of these head+tail features are traced by filamentary $1.64\ \mu\text{m}$ [Fe II] emission (Fig. 2) supports this interpretation and, furthermore, suggests that the velocities of the entraining winds, relative to the clump/tail structures, well exceed $\sim 50\ \text{km s}^{-1}$ (see §5.2).

Four of our WFC3 images were obtained in filters that were also used in previous (epoch 2009) HST/WFC3 imaging of NGC 6302 (specifically, F502N, F656N, F658N, and F673N). The **AstroDrizzle** image registration procedure described in § 2, which exploits field stars common to image pairs, was used to place these WFC3 images into the astrometric coordinate frame of the images in the 2019–2020 WFC3 image suite that were obtained through the corresponding filters. Detailed analysis of the nebular kinematics revealed in difference and ratio images constructed from these multi-epoch images is deferred to a subsequent paper (Balick et al., in preparation). Here we merely note that (a) the lobe clump/tail structures generally display the clearest signs of proper motion of any nebular structures, due to their well-defined head/tail structures; and (b) our difference-image-based analysis of the ballistic expansion of these structures, analogous to that described in Schönberner et al. (2018), indicates that their characteristic dynamical (ejection) timescale is ~ 2000 yr. The latter result is consistent with previous multi-epoch imaging studies of the nebula (Meaburn et al. 2008; Szyszka et al. 2011). However, some inner lobe structures also clearly display proper motions that are of similar magnitude to those of the outer lobe structures, suggestive of more recent mass ejections (see §6).

Beyond the clumps’ bright edges and along the outer edges of their tails, the [O III]/H β ratio drops precipitously (see Fig. 8, E–W profile, and Fig. 10, greyscale insets). In contrast, the [N II]/H α and [S II]/H α ratios both significantly increase within the clumps (again see Fig. 8, E–W profile, and Fig. 10, color panels). On the one hand, this appears to rule out the possibility that the [N II] and [S II] in the clump shadows is produced by stellar UV, since we would expect the optical depths to 10–20 eV photons to be large within the clumps. Ionization behind the clumps may be the result of UV photons released by Lyman-series recombinations; however, such photons must originate in close proximity to the tails in order to penetrate deeply into the shadow zone. Alternatively, these regions may be exhibiting PDR-like behavior, wherein the layers of [N II] and [S II] emission are the result of significant N and S abundance enhancements driven by UV photodissociation of N- and S-bearing molecules along the surfaces of the dusty clumps. Radio interferometric imaging of such molecules (e.g., HCN, CN, SO, SO₂) in the clump regions would test the latter hypothesis.

5.2. The [Fe II] wedges

In each lobe, the region (wedge) of bright [Fe II] lies on the opposite side of the clump wedge from the amorphous wedge (Fig. 9). The $1.64\ \mu\text{m}$ [Fe II] emission line has an excitation temperature of $T_{\text{ex}} \sim 1.1 \times 10^4$ K. As a consequence, $1.64\ \mu\text{m}$ [Fe II] emission is typically a tracer of fast (J-type) shocks. The line has been detected and mapped in a diverse array of astrophysical environments, such as Herbig-Haro objects associated with jets from young stellar objects (e.g., McCoe et al. 2004), the Orion KL Nebula (e.g., Bally et al. 2015), supernova remnants (e.g., Keohane et al. 2007), and active galactic nuclei (e.g., Forbes & Ward 1993); all of these systems feature shock speeds in excess of $\sim 50\ \text{km s}^{-1}$ and often $>100\ \text{km s}^{-1}$. However, images of PNe in this line are few and far between (e.g., M2-9; Balick et al. 2018).

The intensity of the $1.64\ \mu\text{m}$ [Fe II] emission peaks sharply along the edges of these point-symmetric lobe structures (see N–S intensity profiles in lower panels of Fig. 8), indicating that these particular surfaces of the PN lobes are being actively shaped by fast, collimated winds emanating from the immediate vicinity of its central star. The lack of detection of X-rays from NGC 6302 by *Chandra* (Kastner et al. 2012) suggests that the relative wind speed at these [Fe II]-emitting interfaces cannot be much faster than necessary to excite the $1.64\ \mu\text{m}$ line (i.e., ~ 50 – $150\ \text{km s}^{-1}$). More sensitive soft X-ray imaging observations are clearly warranted, however, especially given the detection of emission lines of O VII and O VIII in archival IUE spectra (Feibelman 2001).

5.3. The “amorphous” wedges

In contrast to the “clump” and [Fe II] zones just described, the “amorphous” wedge zones appear less structured, and display weaker $1.64\ \mu\text{m}$ [Fe II] emission (Fig. 9). Dynamically, these amorphous wedges may be “quiet” dynamic zones, unlike the [Fe II] wedge regions (see next). However, the azimuthal locations of the “amorphous” wedges closely coincide with faint, very extended, jet-like structures tentatively detected in wider-field UV imaging (Kameswara Rao et al. 2018). The combination of thin-walled interfaces along the edges of the amorphous zones and the possible UV

detection of larger-scale structures along these same PAs (Kameswara Rao et al. 2018) indicates that fast winds fill these apparently hollow (and seemingly dynamically quiet) lobe interiors and generate shocks along the inner lobe walls.

Sensitive, high-resolution UV spectroscopy is required to confirm the apparent detection of pc-scale, low-surface-brightness UV emission along the amorphous wedge directions by Kameswara Rao et al. (2018) and, if confirmed, to ascertain whether this emission is in fact due to H_2 fluorescence, as proposed by those investigators. If this emission is indeed due to lines of H_2 , such UV spectroscopic measurements might further yield the kinematic signatures of large-scale, collimated outflows. Regardless, if fast winds are indeed flowing through the amorphous wedge regions then — given the symmetry of the amorphous and [Fe II] wedges with respect to the central torus — it stands to reason that these same winds cause the shocks that generate the bright, extended $1.64\ \mu\text{m}$ emission within the [Fe II] wedges. This then begs the question as to why the $1.64\ \mu\text{m}$ [Fe II] line is relatively faint and less extensive within the amorphous wedges. The implication is either that the density within the zone of fast wind flow within the amorphous wedges is lower than that in the [Fe II] wedges, or that the interactions of the fast wind with the lobe walls are more energetic along the N (S) borders of the W (E) lobes, where the strongest [Fe II] emission arises.

5.4. The “gap” wedge

The “gap” wedge is a narrow zone within the west lobe, between the [Fe II] and clump wedges, that displays a lack of structure. The gap wedge seems to be an empty, perhaps jet-evacuated region that connects the inner west lobe to the larger “breakout lobe” structure to the NW (PA $\sim 300^\circ$) that is seen in wide-field images of NGC 6302 (Meaburn et al. 2005; Kameswara Rao et al. 2018). This breakout lobe is expanding at an estimated deprojected $\sim 600\ \text{km s}^{-1}$ in the plane of the sky at $\sim 7'$ from the nebular core (Meaburn et al. 2005). The breakout lobe is also seen to be expanding laterally at $\sim 200\ \text{km s}^{-1}$ (López et al. 2012). This strongly implies that the same collimated flow that generates the “breakout lobe” is also producing the [Fe II]-emitting shocks along the point-symmetric (ESE and WNW) lobe surfaces. The “gap” wedge to the NW of the core region hence may simply be a cowl through which invisible, supersonic, collimated winds flow into the NW breakout lobe. This general scenario has been validated via detailed hydrodynamic modeling of other bipolar pre-PNe and young PNe (Balick et al. 2019). Although both NW and SE breakout lobe structures are detected in far-UV imaging (Kameswara Rao et al. 2018), the SE counterpart to the “gap” wedge is harder to discern in the WFC3 images (Fig. 9).

6. THE CENTRAL STAR: DEEPENING ENIGMA

6.1. The imposter lurking near the core of NGC 6302

As previously noted, we defer analysis of difference images obtained from multi-epoch HST/WFC3 imaging to a future paper. However, we report here on a striking result that is immediately apparent from a difference image obtained from subtracting the previous (2009) F673N image from our new (2020) F673N image. The former WFC3 F673N image was used to identify a star, located near the intersection of the nebula’s waist and its symmetry axis, as the CSPN of NGC 6302 (Szyszka et al. 2009). The central region of the 2009 and 2020 F673N images and the 2020–2009 F673N difference image is presented in Fig. 11. It is immediately apparent that the star that was identified as the CSPN in the first-epoch (2009) WFC3 images in fact shows significant proper motion (PM). Specifically, we measure a position of (RA, dec) 17:13:44.3632, $-37:06:12.774$ for this star at the epoch of the 2020 March 13 HST/WFC3 imaging, vs. 17:13:44.3883, $-37:06:12.874$ on 2009 July 27. This offset ($\sim 0.37''$) translates to a PM of $\sim 35\ \text{mas yr}^{-1}$ at position angle $\sim 285^\circ$. This PM is larger than that measured for any other field star in the F673N image; all other field stars have PMs $< 10\ \text{mas yr}^{-1}$ (an example appears at the far right of the frame in Fig. 11). Furthermore, these small field star PMs are directed randomly, as expected for accurate astrometric alignment. At $D = 1.0\ \text{kpc}$, our adopted distance to NGC 6302, the PM measured for the putative central star identified by Szyszka et al. (2009) would translate to a projected velocity of nearly $200\ \text{km s}^{-1}$ directed transverse to the equatorial plane of the system. This is a physically implausible velocity both for the CSPN of NGC 6302 or for a putative binary companion.

We conclude that the star previously identified as the central star of NGC 6302 is, in fact, unrelated to the nebula. Furthermore, while it is apparent from the prominence of this star in our near-IR WFC3 images that it is quite red, various lines of evidence indicate that this star is most likely a foreground, as opposed to background, field star (the star’s parallax cannot be determined by Gaia, due to NGC 6302’s bright core line emission). From our $0.67\ \mu\text{m}$ (F673N), $1.1\ \mu\text{m}$ (F110W), and $1.6\ \mu\text{m}$ (F160W) images, we obtain magnitudes of 19.67 ± 0.07 , 16.74 ± 0.02 , and 16.15 ± 0.02 , respectively. For distances between $\sim 250\ \text{pc}$ and $\sim 1\ \text{kpc}$, the reddening along the line of sight to NGC

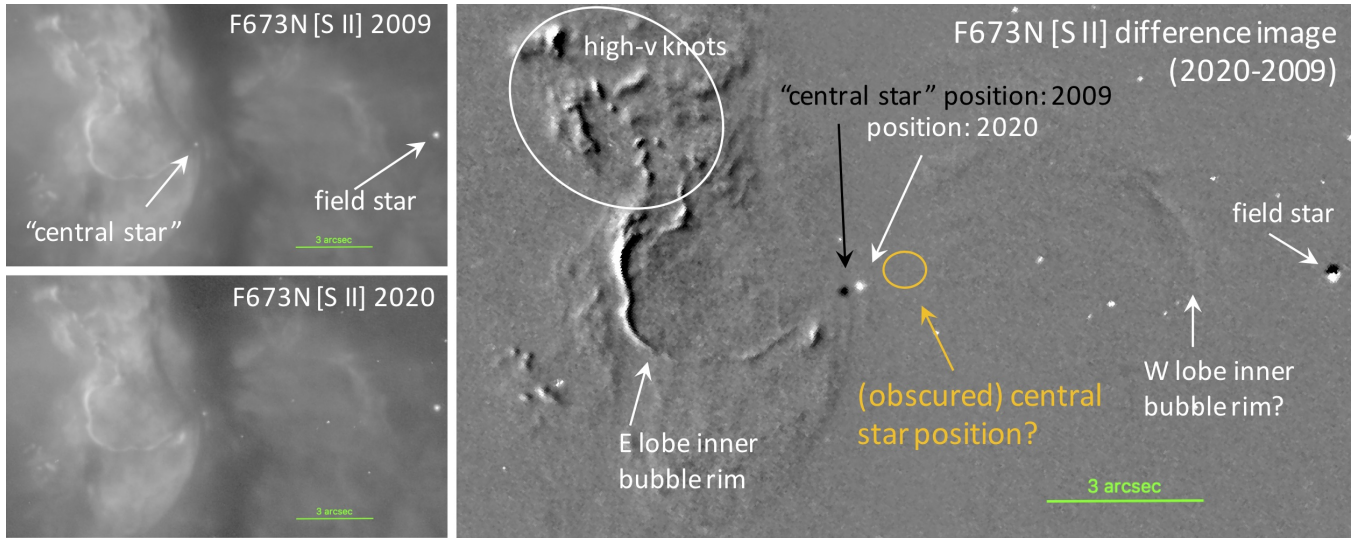


Figure 11. Multi-epoch HST/WFC3 F673N imaging of the central $\sim 17'' \times 10''$ region of NGC 6302. Left panels: F673N images of NGC 6302 obtained in 2009 (top) and in 2020 (bottom). Right panel: 2020–2009 F673N difference image. In each panel, N is up and E to left. The difference image establishes that the star previously identified as the CSPN (Szyszka et al. 2009) exhibits proper motion of $\sim 35 \text{ mas yr}^{-1}$. Note the far smaller (and nearly orthogonal) proper motion of the field star at the far right of the frame. The proposed actual position of the (obscured) central star (17:33:14.30, $-37:06:12.244$), as inferred from the inner lobe (high proper motion, hence black/white) “bubble” features, is indicated with a yellow oval. A system of high-velocity knots (circled) extends to the NE of the inferred central star position. The uncorrected signatures of cosmic rays in the 2020 image appear as compact white spots in the difference image (with sizes less than those of the stellar images).

6302 is $E(B - V) \approx 0.3$ (Lallement et al. 2019), suggesting the dereddened F673N, F110W, and F160W magnitudes are approximately 18.9, 16.5, and 16.0, respectively (Cardelli et al. 1989). Assuming the field star is on the main sequence, these F673N–F110W and F110W–F160W colors (2.4 and 0.5 mag, respectively) indicate an early-M spectral type (Pecaut & Mamajek 2013). We then (crudely) estimate a distance in the range ~ 500 –750 pc. The PM magnitude corresponds to a space velocity of $\sim 85 \text{ km s}^{-1}$ at 500 pc, suggesting that the star may be a high-velocity (possibly Pop II) dwarf. While it is possible the star is instead a cool giant that lies well behind the nebula, and is hence reddened by the dust in the central torus region, this seems unlikely, given the space velocity would then be $\gtrsim 200 \text{ km s}^{-1}$. Furthermore, we measure the same flux for the star (to within $\sim 10\%$) in the two F673N images, despite its (projected) position deeper within the dark lane in the 2020 image. If this were a background star, one might have expected to observe a measureable change in brightness (most likely, a dimming).

6.2. Implications for the properties of the central star and its progenitor

It is truly an unfortunate coincidence that a foreground star displaying the largest PM of any field star in the F673N image field of view is seen projected so near the geometric center (waist) of the bipolar nebula NGC 6302. Obviously it is necessary to discard previous deductions concerning the properties of the central star of NGC 6302 that were based, directly or indirectly, on the properties of this interloping field star. In particular, conclusions concerning the extinction toward the CSPN and the present-day CSPN mass that were based on its apparent direct detection by HST (such as the A_V estimates obtained by Szyszka et al. 2009; Wright et al. 2011) are certainly not reliable. Fortunately, however, most literature determinations of the central star’s luminosity and effective temperature — including those in Szyszka et al. (2009) and Wright et al. (2011) — are based on the total luminosity and excitation of the nebular emission, as opposed to the visible-wavelength photospheric properties of the field star that, we now know, is merely seen in projection toward the nebula’s dark lane.

The newly established absence of the central star in HST imaging also then begs the question: *Where, in fact, is the central star of NGC 6302?* Obviously it is essential to answer this question, given that all the available evidence points to the likelihood that this object is descended from a star that pushed the upper envelope of plausible PN progenitor masses. In particular, the HST/WFC3 images confirm, and further elaborate on, the findings of Rauber et al. (2014) that the $[\text{N II}]/\text{H}\alpha$ ratios of the lobe clumps are unusually high ($[\text{N II}]/\text{H}\alpha \sim 10$; §4.2). This supports previous abundance analyses establishing that both N/H and N/O are very large in NGC 6302 (i.e., super-solar by

factors of ~ 10 and ~ 200 , respectively; Milingo et al. 2010; Rauber et al. 2014), and strongly suggests that the clumps were ejected by a massive, N-enriched central AGB star (Karakas & Lugaro 2016). This inference is consistent with the (large) estimated luminosity and effective temperature of the present-day central star (i.e., $L_\star \gtrsim 4200 L_\odot$, adopting $D = 1.0$ kpc, and $T_{\text{eff}} \sim 220$ kK; Wright et al. 2011). NGC 6302 is also among the most massive known PNe, with total gas mass estimates ranging from $\sim 0.5 M_\odot$ (Dinh-V-Trung et al. 2008) to $\sim 3.5 M_\odot$ (Wright et al. 2011, where this latter estimate has also been corrected for our adopted distance of 1.0 kpc). Estimates of the gas mass in the central torus region alone range from $\sim 0.1 M_\odot$ (Dinh-V-Trung et al. 2008; Santander-García et al. 2017) to as high as $\sim 3 M_\odot$ (Matsuura et al. 2005, but see discussion in Dinh-V-Trung et al. 2008).

One potential clue to the location of the CSPN is offered by the F673N difference image (Fig. 11). Specifically, the east lobe shows a rapidly expanding inner arc or rim of length $\sim 20''$ that is suggestive of the leading edge of a bubble-like structure. There appears to be a faint counterpart to this expanding arc structure within the west lobe. If this pair of high-proper-motion, bubble-like features was produced by simultaneous, oppositely directed mass ejections, then the star could lie at their midpoint. As indicated in Fig. 11, these inner shell features thus suggest the central star is actually located well to the west of the foreground field star, right at the heart of the nebula’s central dark lane/torus, at a position of (RA, dec) 17:33:44.30, $-37:06:12.2$ (where this estimate of the midpoint of the rims of the bubble-like features has an uncertainty of $\sim 0.5''$). A system of high-PM knots, apparent in the F673N difference image (see Fig. 11), appears to emanate from near this same position. No point source is detected at this position in our HST/WFC3 images, however — even in the near-IR (at wavelengths as long as $\sim 1.6 \mu\text{m}$) — suggesting that $A_V \gg 10$ (see discussion in Wright et al. 2011). In future work, we will test this predicted central star position, via determination of the expansion center of the nebula as well as analysis of archival ALMA data (Santander-García et al. 2017).

6.3. What happened at the core of NGC 6302?

All of the preceding lines of evidence — NGC 6302’s highly elevated N/H abundance ratio, the large luminosity and effective temperature of its central star, and its large inferred nebular mass — support the hypothesis that the present-day NGC 6302 nebula was generated by a star of initial mass $\sim 5\text{--}8 M_\odot$. Such a star represents the upper end of the progenitor mass range that can generate a PN, as opposed to exploding as a supernova. Apparently the bulk of the mass of this behemoth of a progenitor star was ejected over the past $\sim 2000\text{--}5000$ yr (Meaburn et al. 2008; Santander-García et al. 2017), implying a mass loss rate exceeding $10^{-4} M_\odot \text{ yr}^{-1}$. This would far surpass the mass loss rates typically observed for even the most luminous AGB stars (Höfner & Olofsson 2018). Furthermore, models predict that the evolutionary timescales of PN central stars as massive, luminous, and hot as the CSPN of NGC 6302 are on the order of centuries (e.g., Miller Bertolami 2016). It is hence clear that — as has been previously speculated by various investigators over the past four decades (e.g., Aller et al. 1981; Meaburn et al. 2008; Wright et al. 2011; Szyszka et al. 2011) — we are likely witnessing NGC 6302 at a key, highly transient evolutionary period immediately following a highly disruptive event, or perhaps series of events, in the recent history of its central star system. Use of the term “central star system” in this context is intentional (and essential) since, as noted in the Introduction, generation of pronounced bipolar structure, as observed in NGC 6302, most likely ultimately requires the presence of a close binary companion to the PN central star⁵.

Combining the qualitative analysis presented in §5 with the results of previous investigations of the structure and kinematics of NGC 6302, there is evidence that distinct episodes of such interacting-binary-influenced mass loss have led to the nebula we presently observe. Specifically, the dusty, molecule-rich torus that defines the equatorial plane of the system was evidently ejected, at low speed ($\sim 10 \text{ km s}^{-1}$), $\sim 5000\text{--}7500$ years prior to the present observing epoch (Peretto et al. 2007; Santander-García et al. 2017). The N-rich clumps within the nebular lobes were then ejected in a dense but faster ($\sim 100 \text{ km s}^{-1}$) bipolar wind that was initiated some ~ 3000 years after the ejection of the equatorial torus (Szyszka et al. 2011). The ejection of these lobe clump structures was accompanied or closely followed by much faster ($\sim 600 \text{ km s}^{-1}$) winds along the “gap” and (possibly) “amorphous” directions (see Fig. 9); the ($\sim 2000\text{--}2500$ yr) dynamical ages of these far larger lobe/jet structures (Meaburn et al. 2008)⁶ are similar to that of the ejection timescale of the lobe clumps. Our new HST/WFC3 imaging detection of extensive [Fe II]-emitting shocks along the lobe walls and, to a lesser extent, within the “clump” and “amorphous” regions of the lobes has now revealed that this

⁵ Intriguingly, Feibelman (2001) identified excess UV continuum and Mg II emission from the central region of NGC 6302, and commented that these emission sources were suggestive of the presence of a G-type companion to the central star.

⁶ Kameswara Rao et al. (2018) deduce dynamical ages of ~ 10 kyr for the UV-imaged lobe/jet structures on the basis of an assumed outflow velocity of 160 km s^{-1} , a factor ~ 4 smaller than measured for the extended NW lobe structure of NGC 6302 (Meaburn et al. 2005).

most recent stage of fast ($\gtrsim 100 \text{ km s}^{-1}$) winds — i.e., collimated and, possibly, precessing outflows from the putative binary system at NGC 6302’s core region — is ongoing. Finally, we note that, according to models that simulate the formation of bipolar PNe, the foregoing episodes of directed mass loss likely would have been preceded by a sustained period of more or less isotropic AGB mass loss at lower rates (Lee & Sahai 2003; Huarte-Espinosa et al. 2012; Balick et al. 2019). The extant data do not provide any direct evidence of this phase of quiescent mass loss, though they also do not rule out such a phase.

Development of a self-consistent physical model of the rapid evolution of NGC 6302 that can account for all of these structural and kinematic elements is beyond the scope of this paper. We instead briefly consider two models, both involving interacting binary systems, that have been proposed to lead to abruptly transformative episodes during late (AGB) evolutionary stages of the primary star (the first of which having been proposed to apply specifically to NGC 6302, among other nebulae): (1) a so-called intermediate luminosity optical transient (ILOT) event, and (2) onset of common envelope evolution.

Soker & Kashi (2012) have hypothesized that NGC 6302 and a handful of similarly extreme bipolar nebulae may have undergone ILOT events, during which much of the mass in their bipolar lobes was ejected. Such ILOTs, which are intermediate in luminosity between novae and supernovae, have been observed in a few extragalactic sources and luminous blue variables (LBVs). Soker & Kashi (2012) point out that the kinetic energy represented by the lobes of NGC 6302 is similar to the former class of eruptive object, whose members (collectively) lie along a “stripe” of energy-timescale parameter space connecting them to LBVs. In relating NGC 6302 to ILOT sources, they describe a scenario in which an AGB star with a main-sequence companion in a (possibly eccentric) few-au orbit undergoes short-lived, binary-interaction-driven phases of instability, during which the AGB star is prone to lose mass at high rates. Soker & Kashi (2012) speculate that, prior to the ILOT episode, an interaction of the AGB star and companion (involving no Roche Lobe overflow) resulted in the formation of the NGC 6302 equatorial torus. Subsequently — a few $\times 10^3$ yr after torus formation, given the “timeline” of NGC 6302’s mass loss episodes described above — a second binary encounter, or series of encounters over a $\lesssim 100$ yr period, led to Roche Lobe overflow. As a result, some fraction of the mass ejected during this second encounter was captured in an accretion disk around the companion, leading to the formation of transient, accretion-powered jets. The resulting ILOT then generated the bipolar lobes over this same relatively short period.

If this ILOT-based model indeed describes the formation of NGC 6302, then it would remain to explain the presence of the extensive (~ 0.3 pc-scale), point-symmetric regions of active shocks in the nebula that have now been revealed by our $1.64 \mu\text{m}$ [Fe II] imaging (Fig 2). That is, if these [Fe II]-emitting shocks and the many other point-symmetric features within this nebula that are apparent in our imaging and in various previous imaging studies of this nebula (e.g., Szyszkta et al. 2011; Kameswara Rao et al. 2018) are generated by (possibly precessing) jets from a binary companion’s accretion disk, then clearly the resulting wind interactions that have shaped NGC 6302 are ongoing. Furthermore, the region of NGC 6302 within $\sim 20''$ of the central dark lane (faint circle in Fig. 9) features a system of nested bubbles and knots with large PMs, oriented at a range of PAs, that appear to emanate from the presumed position of the CSPN (Fig. 11). This (presumably) younger, “multipolar” core region somewhat resembles the complex cores of the bipolar nebulae Hubble 5 and NGC 2440 (Corradi & Schwarz 1993; Lago & Costa 2016). All of the above features of the nebula suggest that accretion processes are still active in the central binary system within NGC 6302.

Alternatively, it is possible that NGC 6302 is the result of the onset of a common envelope (CE) stage in the evolution of a close binary system, a scenario also considered by Kameswara Rao et al. (2018). Recent simulations have shown that such a CE event can result in formation of a dense toroidal structure, which can in turn serve as an effective collimator for a subsequent fast wind from the central, merged binary remnant (García-Segura et al. 2018; Zou et al. 2020). This configuration results in simulated bipolar nebulae with structural features (i.e., torus, lobes, shocks) that overall resemble those observed in NGC 6302. However, as noted, the generation of large outer lobe structures and point-symmetry that characterize NGC 6302 likely requires pre-existing and ongoing jet activity, respectively, which in turn points to the influence of binary interactions prior to and following the common envelope phase (see García-Segura et al. 2018).

7. SUMMARY AND CONCLUSIONS

We have presented the results of a comprehensive, near-UV-to-near-IR Hubble Space Telescope WFC3 imaging study of the young planetary nebula (PN) NGC 6302, the archetype of the class of extreme bi-lobed, pinched-waist PNe that are rich in dust and molecular gas. The new WFC3 emission-line image suite clearly defines the dusty toroidal equatorial structure that bisects NGC 6302’s polar lobes, and the fine structures (clumps, knots, and filaments) within the lobes. The most striking and unexpected aspect of the new WFC3 image suite is the bright, S-shaped $1.64\ \mu\text{m}$ [Fe II] emission that traces the southern interior of the east lobe rim and the northern interior of the west lobe rim, in point-symmetric fashion, which we interpret as a zone of shocks caused by ongoing, fast ($\gtrsim 100\ \text{km s}^{-1}$), collimated winds from NGC 6302’s central star(s).

The [Fe II] emission zone represents one of a handful of regions beyond $\sim 20''$ from the central dark lane that appear as distinct azimuthal zones (wedges) within the nebula. In addition to the [Fe II] zone, these wedges comprise a region featuring dense knots with outward facing features and tails along the nebular symmetry axis; a dark wedge with traces of dust-scattered light along the nebular minor axis; and a zone with radial streaks or amorphous structure in between. The boundaries between these wedge-shaped regions are marked by strong azimuthal gradients in nebular ionization structure.

These new (2019+2020) WFC3 images also reveal that the object previously identified as NGC 6302’s central star (on the basis of 2009 HST/WFC3 imaging) is in fact a foreground field star. We propose that a pair of bubble-like features in the nebula’s core region instead likely pinpoints the central star’s actual position within the nebula’s dusty central torus. The available evidence indicates that this star is descended from a progenitor near the upper end of the mass range that could generate a PN, as opposed to exploding as a supernova.

The features revealed by our panchromatic HST/WFC3 images of NGC 6302 — in particular, its distinct azimuthal structural zones and nested bubble system, and the surprising misalignment of the central engine’s present collimated fast wind direction (as traced by $1.64\ \mu\text{m}$ [Fe II] emission) and the nebula’s main axis of symmetry (as defined by its dusty molecular torus, polar-axis clump system, and outer lobe walls) — presents an especially daunting challenge for models of the origin and evolution of bipolar structures in PNe. The presence of an interacting binary companion to the central former AGB star, leading to formation of a disk/jet system, appears to be a requirement of such a model. It may be impossible to establish whether one star or two stars now lie at the core of NGC 6302, given the enormous extinction to and luminosity of its central star system. Nonetheless, additional observations that can pinpoint the central star(s) are clearly warranted. In particular, subarcsecond-resolution observations in the mid-IR (JWST) and submm (ALMA) should lead to far more stringent constraints on both the position and energetics of the central powering source of this enigmatic nebula.

ACKNOWLEDGMENTS

Based on observations made with the NASA/ESA Hubble Space Telescope, obtained at the Space Telescope Science Institute (STScI), which is operated by the Association of Universities for Research in Astronomy, Inc., under NASA contract NAS5-26555. These observations are associated with program #15953. Support for this program was provided by NASA through STScI grant HST-GO-15953.001-A to RIT. The authors wish to thank Jeremy Walsh, Stavros Akros, and the anonymous referee for comments that improved this manuscript.

REFERENCES

- | | |
|--|--|
| Akashi, M., & Soker, N. 2018, <i>MNRAS</i> , 481, 2754 | Balick, B., Frank, A., Liu, B., & Corradi, R. 2018, <i>ApJ</i> , 853, 168 |
| Alexander, J., & Balick, B. 1997, <i>AJ</i> , 114, 713 | Bally, J., Ginsburg, A., Silvia, D., & Youngblood, A. 2015, <i>A&A</i> , 579, A130 |
| Aller, L. H., Ross, J. E., Omara, B. J., & Keyes, C. D. 1981, <i>MNRAS</i> , 197, 95 | Bublitz, J., Kastner, J. H., Santander-García, M., et al. 2019, <i>A&A</i> , 625, A101 |
| Ashley, M. C. B., & Hyland, A. R. 1988, <i>ApJ</i> , 331, 532 | Bujarrabal, V., Castro-Carrizo, A., Alcolea, J., & Sánchez Contreras, C. 2001, <i>A&A</i> , 377, 868 |
| Bachiller, R., Forveille, T., Huggins, P. J., & Cox, P. 1997, <i>A&A</i> , 324, 1123 | |
| Balick, B., & Frank, A. 2002, <i>ARA&A</i> , 40, 439 | |
| Balick, B., Frank, A., & Liu, B. 2019, <i>ApJ</i> , 877, 30 | |

- Cardelli, J. A., Clayton, G. C., & Mathis, J. S. 1989, *ApJ*, 345, 245
- Casassus, S., Roche, P. F., & Barlow, M. J. 2000, *MNRAS*, 314, 657
- Casassus, S., Roche, P. F., Barlow, M. J., & Binette, L. 2002, in *Revista Mexicana de Astronomía y Astrofísica Conference Series*, Vol. 12, *Revista Mexicana de Astronomía y Astrofísica Conference Series*, ed. W. J. Henney, J. Franco, & M. Martos, 132–133
- Chen, Z., Frank, A., Blackman, E. G., Nordhaus, J., & Carroll-Nellenback, J. 2017, *MNRAS*, 468, 4465
- Corradi, R. L. M., & Schwarz, H. E. 1993, *A&A*, 269, 462
- Corradi, R. L. M., & Schwarz, H. E. 1995, *A&A*, 293, 871
- De Marco, O., & Izzard, R. G. 2017, *PASA*, 34, e001
- Dinh-V-Trung, Bujarrabal, V., Castro-Carrizo, A., Lim, J., & Kwok, S. 2008, *ApJ*, 673, 934
- Feibelman, W. A. 2001, *ApJ*, 550, 785
- Forbes, D. A., & Ward, M. J. 1993, *ApJ*, 416, 150
- García-Segura, G., Ricker, P. M., & Taam, R. E. 2018, *ApJ*, 860, 19
- Gómez-Gordillo, S., Akas, S., Gonçalves, D. R., & Steffen, W. 2020, *MNRAS*, 492, 4097
- Groves, B., Dopita, M. A., Williams, R. E., & Hua, C.-T. 2002, *PASA*, 19, 425
- Hartigan, P., Morse, J. A., & Raymond, J. 1994, *ApJ*, 436, 125
- Höfner, S., & Olofsson, H. 2018, *A&A Rv*, 26, 1
- Huarte-Espinosa, M., Frank, A., Balick, B., et al. 2012, *MNRAS*, 424, 2055
- Huggins, P. J., Bachiller, R., Cox, P., & Forveille, T. 1996, *A&A*, 315, 284
- Huggins, P. J., Bachiller, R., Planesas, P., Forveille, T., & Cox, P. 2005, *ApJS*, 160, 272
- Jones, D., & Boffin, H. M. J. 2017, *Nature Astronomy*, 1, 0117
- Kameswara Rao, N., De Marco, O., Krishna, S., et al. 2018, *A&A*, 620, A138
- Karakas, A. I., & Lugaro, M. 2016, *ApJ*, 825, 26
- Kastner, J. H., Bublitz, J., Balick, B., et al. 2020, *Galaxies*, 8, 49
- Kastner, J. H., Weintraub, D. A., Gately, I., Merrill, K. M., & Probst, R. G. 1996, *ApJ*, 462, 777
- Kastner, J. H., Montez, R., J., Balick, B., et al. 2012, *AJ*, 144, 58
- Kemper, F., Molster, F. J., Jäger, C., & Waters, L. B. F. M. 2002, *A&A*, 394, 679
- Keohane, J. W., Reach, W. T., Rho, J., & Jarrett, T. H. 2007, *ApJ*, 654, 938
- Kwitter, K. B., Méndez, R. H., Peña, M., et al. 2014, *RMxAA*, 50, 203
- Kwok, S., Purton, C. R., & Fitzgerald, P. M. 1978, *ApJ*, 219, L125
- Lago, P. J. A., & Costa, R. D. D. 2016, *RMxAA*, 52, 329
- Lago, P. J. A., Costa, R. D. D., Faúndez-Abans, M., & Maciel, W. J. 2019, *MNRAS*, 489, 2923
- Lallement, R., Babusiaux, C., Vergely, J. L., et al. 2019, *A&A*, 625, A135
- Lee, C.-F., & Sahai, R. 2003, *ApJ*, 586, 319
- Livio, M., Salzman, J., & Shaviv, G. 1979, *MNRAS*, 188, 1
- López, J. A., Richer, M. G., García-Díaz, M. T., et al. 2012, *RMxAA*, 48, 3
- Matsuura, M., Zijlstra, A. A., Molster, F. J., et al. 2005, *MNRAS*, 359, 383
- McCoey, C., Giannini, T., Flower, D. R., & Caratti o Garatti, A. 2004, *MNRAS*, 353, 813
- Meaburn, J., Lloyd, M., Vaytet, N. M. H., & López, J. A. 2008, *MNRAS*, 385, 269
- Meaburn, J., López, J. A., Steffen, W., Graham, M. F., & Holloway, A. J. 2005, *AJ*, 130, 2303
- Milingo, J. B., Kwitter, K. B., Henry, R. B. C., & Souza, S. P. 2010, *ApJ*, 711, 619
- Miller Bertolami, M. M. 2016, *A&A*, 588, A25
- Molster, F. J., Lim, T. L., Sylvester, R. J., et al. 2001, *A&A*, 372, 165
- Morris, M. 1987, *PASP*, 99, 1115
- O’dell, C. R., & Handron, K. D. 1996, *AJ*, 111, 1630
- Osterbrock, D. E., & Ferland, G. J. 2006, *Astrophysics of gaseous nebulae and active galactic nuclei*
- Pecaut, M. J., & Mamajek, E. E. 2013, *ApJS*, 208, 9
- Peretto, N., Fuller, G., Zijlstra, A., & Patel, N. 2007, *A&A*, 473, 207
- Raga, A. C., Riera, A., Mellema, G., Esquivel, A., & Velázquez, P. F. 2008, *A&A*, 489, 1141
- Rauber, A. B., Copetti, M. V. F., & Krabbe, A. C. 2014, *A&A*, 563, A42
- Sahai, R., Morris, M. R., & Villar, G. G. 2011, *ApJ*, 141, 31
- Sahai, R., & Trauger, J. T. 1998, *AJ*, 116, 1357
- Santander-García, M., Bujarrabal, V., Alcolea, J., et al. 2017, *A&A*, 597, A27
- Schoenberner, D. 1986, *A&A*, 169, 189
- Schönberner, D., Balick, B., & Jacob, R. 2018, *A&A*, 609, A126
- Soker, N. 2004, *NewA*, 9, 399
- Soker, N., & Kashi, A. 2012, *ApJ*, 746, 100
- Soker, N., & Livio, M. 1994, *ApJ*, 421, 219
- Speck, A. K., Meixner, M., Jacoby, G. H., & Knezek, P. M. 2003, *PASP*, 115, 170
- Szyszkka, C., Walsh, J. R., Zijlstra, A. A., & Tsamis, Y. G. 2009, *ApJL*, 707, L32

Szyszkla, C., Zijlstra, A. A., & Walsh, J. R. 2011, MNRAS, 416, 715
Wright, N. J., Barlow, M. J., Ercolano, B., & Rauch, T. 2011, MNRAS, 418, 370

Zou, Y., Frank, A., Chen, Z., et al. 2020, MNRAS, 497, 2855